8th AIAA/ASME Joint Thermophysics and Heat Transfer Conference
24-26 June 2002, St. Louis, Missouri

AIAA 2002–3308

Turbulence Model Validation for Hypersonic Flows

James L. Brown
NASA Ames Research Center, Moffett Field, CA 94035

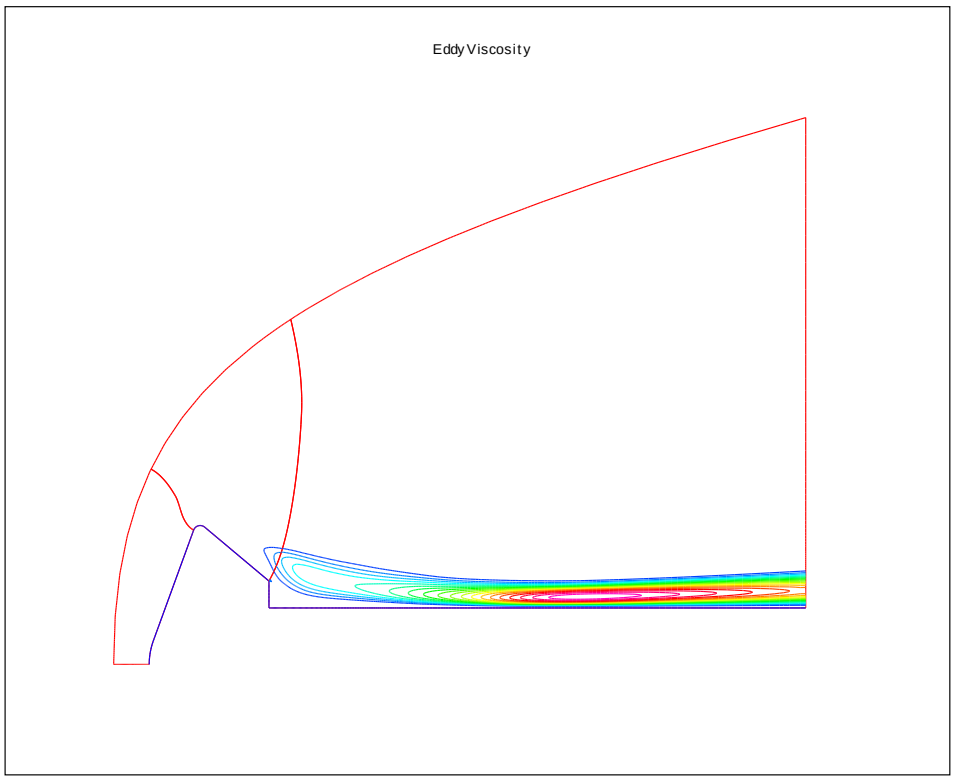

8th AIAA/ASME Joint Thermophysics and Heat Transfer Conference June 24–26, 2002/St Louis, MO

Turbulence Model Validation for Hypersonic Flows

James L. Brown*
NASA Ames Research Center, Moffett Field, CA 94035

Accurate computation of the aerothermal environment about atmospheric entry vehicles is crucial to the design of thermal protection systems for planetary probe missions. In order to enhance the fidelity of available computational heat transfer capability, the SST (Shear-Stress Transport) and the 1998 Wilcox two-equation $k-\omega$ eddy-viscosity turbulence models, along with compressibility corrections and a means to specify transition, are incorporated into a real-gas Navier-Stokes code. The ability of these models and code to accurately compute hypersonic flows is assessed through a turbulence model validation process. Emphasized in this process is the assessment and evaluation of the turbulence models in prediction of heat transfer as applied to a range of hypersonic flows selected as characteristic of atmospheric entry vehicles. The flows considered are cold-wall with a range in Mach number from a Mach 7, 3D experiment to an axisymmetric Mach 20 flight experiment. Agreement with established engineering correlations is also examined. The validation provided in this study is not only an assessment of the heat transfer predictive capability of the turbulence models considered, as applied to the hypersonic regime, but also is a verification of the particular implementation of these models into a particular real-gas Navier-Stokes code. This assessment will be of value in establishing factors of safety for the design of thermal protection systems of future aero-capture and aero-braking space vehicles.

Nomenclature

a	sound speed, m/s
c_p	specific heat at constant pressure, J/kg·K
C_f	skin friction coefficient, $2\tau_w/\rho_e U_e^2$
C_h	heat transfer coefficient, $q_w/\rho_\infty U_\infty(H_\infty - h_w)$
h	specific enthalpy, J/kg
H	specific total enthalpy, J/kg
k	turbulent kinetic energy, $(u'^2 + v'^2 + w'^2)/2$
$\mathcal{K}$	thermal conductivity, W/m·K
M	Mach number
M_T	turbulent Mach number, $\sqrt{2k}/a$
p	static pressure, Pa
p_t	total pressure, Pa
Pr	Prandtl Number, $\mu c_p/\mathcal{K}$
q	heat flux per unit area, W/m^2
Re_x	Reynolds number based on length x
R_f	Reynolds analogy number, $2St/C_f$
s	arc length, m
St	Stanton number, $q_w/\rho_e U_e(h_{aw} - h_w)$
t	time, s
T	static temperature, K
T_{aw}	adiabatic wall temperature, K
T_t	total temperature, K
u, v, w	Cartesian velocities, m/s
u', v', w'	turbulent velocities, m/s
u^+	u/u_τ
u_τ	wall friction velocity, m/s
U	velocity, m/s
x, y, z	Cartesian body axes, m
y^+	$\rho u_\tau y/\mu$
ϵ	turbulent kinetic energy dissipation rate
μ	dynamic viscosity, kg/m·s
ν	kinematic viscosity, μ/ρ, m^2/s
ρ	density, kg/m^3
τ_w	wall shear stress, Pa
θ	momentum thickness (compressible), m
ω	specific dissipation, $\epsilon/(0.09k)$, s^{-1}
Ω	magnitude of mean vorticity vector, s^{-1}

Subscripts

aw	adiabatic wall
e	edge conditions
t	total conditions
w	wall
∞	freestream conditions

Introduction

VEHICLES designed to enter a planetary atmosphere undergo a wide range of fluid mechanic regimes, ranging from non-continuum to continuum, reacting real gas to perfect gas, hypersonic to low supersonic, laminar, transitional and turbulent. The heating over the entire vehicle must be predicted with confidence and accuracy. Though such vehicles often are of a relatively simple geometric configuration, the wide range of flight conditions presents a challenge for the predictive methods used. Peak heating for

*Research Scientist, Reacting Flow Environments Branch, Space Technology Division. Member, AIAA.

atmosphere entry trajectories typically occurs at hypersonic speeds and may occur with either transitional or turbulent flow. Also, the bulk of the total heat load to the vehicle thermal protection system (TPS) can occur while flow over the vehicle is in a transitional or turbulent hypersonic regime. Design of the thermal protection system requires a conservative approach, yet an overly conservative prediction of heat transfer and total heat load will unnecessarily increase TPS mass at the expense of payload mass. Further, the placement (and thickness) of thermal protection can affect center of gravity and, thus, aerodynamic stability. In order to ensure accurate thermal predictions, the present work examines the suitability of various turbulence models for a range of conditions and for flows typically encountered by entry vehicles. The paper also describes details required for implementation of these turbulence models into a real-gas Navier-Stokes code which is currently used in defining the aerothermal environment around entry vehicles.

Current practice for planetary entry vehicle design subject to turbulent hypersonic flows has typically relied on the use of the Baldwin-Lomax algebraic turbulence model modified for compressible flows. The clear advantages of one- and two-equation turbulence models demonstrated for transonic aerodynamic flows motivates their consideration for hypersonic flows as well. The turbulence models emphasized here include the compressible form of the Baldwin-Lomax[1] algebraic and several $k-\omega$ two-equation model variants, including the 1988 and 1998 versions of the Wilcox $k-\omega$ model[2,3] and Menter's SST turbulence model.[4,5] Considered also are the Spalart-Allmaras[6,7] one-equation model, and the Chien[8] $k-\epsilon$ two-equation model. Compressibility corrections are incorporated into the $k-\omega$ models. Predictive capability for heat transfer relative to the current form of the widely-used Baldwin-Lomax model is a primary consideration in this evaluation.

Computational Methods

Solutions for the current study were obtained using the *GASP* code.[9] This commercially available Navier-Stokes code (developed by AeroSoft, Inc.) is a three-dimensional (3D) finite-volume code, which incorporates numerous options. The options available include modeling of gas chemistry, real-gas properties, inviscid flux formulation, numerical integration algorithms and boundary conditions. The real-gas ability in *GASP* is of particular interest when solving planetary atmospheric entry problems.

Upwind flux options may be specified separately for each of the three coordinate directions and include the Van Leer,[10] Roe[11] and AUSM$^+$ [12] inviscid flux formulations. Most useful for hypersonic interactions is the mixed VL2R option where the Van Leer inviscid flux formulation is used in the streamwise and spanwise direction and the Roe flux formulation is used in the wall-normal direction. Also proven useful has been the AUSM$^+$ flux formulation option applied in all three directions. Also considered is the VL3 option where the Van Leer flux formulation option is used for all three directions. Formal third-order spatial accuracy for the inviscid fluxes is achieved by means of the MUSCL scheme.[10] The minmod limiter is used for all calculations reported. Time-advancement of 3D flowfields to steady-state solutions may be accomplished with either a 2D Approximate Factorization (AF2) with planar relaxation option or with a point-Jacobi algorithm with inner iterations. These two time-advancement options have proven to perform nearly identical in convergence, robustness and speed.

Additionally, considerable in-house modifications have been incorporated at NASA Ames Research Center (ARC) to tailor the *GASP* code for the specialized purpose of predicting aerothermal environments around hypersonic atmospheric entry vehicles. The need to robustly compute strong shocks with planetary atmospheric chemistry and the requirement for accurate heat transfer predictions for laminar, transitional and turbulent flows has led to development of the present code, which is an ARC modification of v3.2.6 of *GASP*. This code, and related versions thereof, is used at NASA Ames in predicting aerothermal environments around spacecraft with missions to Mars and other solar system bodies. As such, it is important to continually validate the code along with the various turbulence model implementations against the best of available experimental hypersonic heat transfer data.

In-house modifications to the v3.2.6 version of *GASP* accomplished for the present work included an extensive rewriting of the turbulence subroutines with an emphasis on compressible forms of the Baldwin-Lomax and variants of the two-equation $k-\omega$ model. Also added were Menter's SST turbulence model and the 1998 version of Wilcox's $k-\omega$ turbulence model. Compressibility corrections to these models were also incorporated. Furthermore, implementation of a simple means to specify transition was accomplished. The de-coupled form of the two-equation $k-\omega$ turbulence models was also reworked for speed and robustness. Minor re-writing of the AUSM$^+$ flux option and the AF2 and point-Jacobi time-advancement routines were also accomplished to promote robustness when applied to hypersonic flows.

Turbulence Models

The turbulence models considered for this paper are the compressible Baldwin-Lomax algebraic turbulence model,[1] the 1988 $k-\omega$ (KW88, see Wilcox[2]), the 1998 $k-\omega$ (KW98, see Wilcox[3]), the SST (see Menter[4,5]) and the $k-\epsilon$ (see Chien[8]) two-equation turbulence models. Additionally, some solutions are obtained using the Spalart-Allmaras[6,7] turbulence model with the

CFL3D Navier-Stokes code.[13] The details of the several $k-\omega$ models are given in the Appendix.

The KW88, KW98 and the SST models are variants of the basic $k-\omega$ two-equation turbulence model. They are implemented in *GASP* so as to run either coupled or uncoupled with the mean-flow Navier-Stokes equations. The results reported here were obtained with these $k-\omega$ models uncoupled. Although the turbulent kinetic energy is included in the energy equation for hypersonic flows, the coupling of the $k-\omega$ models to the mean flow equations appears to be sufficiently weak that a coupled solution approach is not needed. Tests on the problems considered in this paper indicate that there exists no particular advantage to coupling the solution of the $k-\omega$ turbulence model equation to the solution of the mean flow equations. Comparisons between coupled and uncoupled methods for the $k-\omega$ models indicate that the solutions are nearly identical, with the uncoupled mode being considerably faster and equally robust. For a perfect gas problem, using the point-Jacobi algorithm, a coupled solution approach involves inversion of a 7×7 matrix (49 work units), whereas an uncoupled solution approach results in inversion of a 5×5 matrix and a 2×2 matrix (29 work units). The $k-\epsilon$ model, however, at present, only runs coupled with the mean-flow equations, (see remarks of Sinha and Candler[14]).

An additional advantage to the uncoupled implementation of the $k-\omega$ and SST turbulence models is that the turbulence equations need not be solved every mean flow iteration. Tests indicate that freezing the turbulence solution for 5 or more mean flow iterations, while also increasing the CFL used for the turbulent equations by the same factor, leads to essentially the same final steady-state solution with a considerable reduction in the overhead associated with two-equation models. Robustness of the solution does not appear hindered. Regardless of this advantage, all solutions shown in this paper obtained with the two-equation $k-\omega$ or SST equations were solved uncoupled but with a turbulence equation iteration occurring every mean flow iteration.

Some description of model implementation seems appropriate. First, the convective flux terms appearing in the k and ω equations are evaluated using a first-order upwind flux treatment (Van Leer, Roe or AUSM$^+$) consistent with the mean flow equations.

Next, for the SST turbulence model, a blending function, F_1, is defined (see Appendix) so as to vary smoothly from a value of 1 near a wall through the log-law region of the boundary layer to a value of 0 for the outer "wake" region of the boundary layer and for free shear layers. This blending function played a critical role in Menter's design of the SST model, where the intent was to use the KW88 model for the inner wall regions of a boundary layer and then use a transformed $k-\epsilon$ model for the outer boundary layer regions and for free shear layers.

In the process of formal transformation of the $k-\epsilon$ turbulence equations, a "cross-diffusion" source term, $(2\rho\sigma_{\omega,2}/\omega)(\partial k/\partial x_i)(\partial\omega/\partial x_i)$, appears in the ω equation for the SST model. This cross-diffusion source term is intended to be inactive near the wall, and so is multiplied by the term $(1-F_1)$.

Note that the cross-diffusion derivative term, $(\partial k/\partial x_i)(\partial\omega/\partial x_i)$, will always be negative close to a wall, where with increasing distance from a wall, k is initially increasing while ω is decreasing. The blending function, F_1, is defined so as to be equal to 1 for the inner wall region of a boundary layer where the cross-diffusion derivative term is negative. Hence, the cross-diffusion source term appearing in the SST ω equation, being multiplied by $(1-F_1)$, will not take on a negative value for a realistic turbulent shear layer. This greatly simplifies the implementation of the SST model into an implicit code since, according to both Wilcox[3] and to Bardina et al.,[15] inclusion of the Jacobian of production-like terms into the implicit matrix to be inverted is to be avoided since to do so reduces diagonal dominance of the implicit matrix and contributes to instability of the implicit algorithm. Therefore, the cross-diffusion source term in the SST ω equation needs only to be treated explicitly.

Another consideration is that the numerical evaluation of a cell-volume average of the cross-diffusion derivative term, $((\partial k/\partial x_i)\ (\partial\omega/\partial x_i))$, is required for both the SST and the KW98 models. This term is evaluated, as with other cell-volume averaged derivatives, using the gradient theorem.[16]

Compressibility Corrections

Corrections for compressibility effects are incorporated as options into both the SST and the 1998 $k-\omega$ turbulence models. The primary effect considered here is a correction needed to account for the reduction in a free shear layer growth due to compressibility, see Birch and Eggers.[17] Wilcox[3] describes a modification to the corrections of Sarkar et al.[18] and of Zeman[19] where the dissipation of k increases with turbulent Mach number, $\sqrt{2k}/a$, and the dissipation of ω decreases with turbulent Mach number, according to:

$$D_{k,c} = D_k(1+1.5F(M_T)),\ \text{and} \quad (1)$$

$$D_{\omega,c} = D_\omega(1-1.5(\beta_k/\beta_\omega)F(M_T)) \quad (2)$$

Where,

$$F(M_T) = \begin{cases} |M_T^2 - M_{T0}^2|, & \text{if } M_T^2 > M_{T0}^2 \\ 0, & \text{otherwise} \end{cases} \quad (3)$$

$$M_T^2 = 2k/a^2,\ \text{and}\ M_{T0} = 1/4. \quad (4)$$

The M_{T0} term was introduced by Wilcox so these corrections would be active in compressible free shear layers, where the turbulent Mach number is high, but inactive in the near wall region of boundary layer

flows where the turbulent Mach number tends to be lower. Wilcox verified the behavior of this correction to both free mixing layers and boundary layer flows up to Mach 5. For this study, the KW98c turbulence model is specified as being the Wilcox 1998 $k-\omega$ model with the Wilcox compressibility correction. Also, the SSTc1 turbulence model is specified as being the SST turbulence model with the Wilcox compressibility correction.

For turbulent boundary layers above Mach 5, the turbulent Mach number can easily exceed M_{T0}, leading to a significant reduction in skin friction and heat transfer predicted for high Mach number turbulent boundary layers when using the KW98c and SSTc1 turbulent models. In order to allow use of the compressibility correction for Mach number above 5, the Wilcox compressibility correction is modified by a redefinition of the turbulent Mach number to create the SSTc2 turbulence model option, where:

$$F(\tilde{M}_T) = \begin{cases} |\tilde{M}_T^2 - M_{T0}^2|, & \text{if } \tilde{M}_T^2 > M_{T0}^2 \\ 0, & \text{otherwise} \end{cases} \quad (5)$$

$$\tilde{M}_T^2 = (2k/a^2)(1-F_1), \text{ and } M_{T0} = 1/4. \quad (6)$$

The F_1 function is already defined for the SST model and has the advantage of being a logical indicator of whether the immediate region is the near wall region of a turbulent boundary layer. The result is that for the SSTc2 turbulence model, the compressibility correction is applied only outside of the near wall region of a turbulent boundary layer, regardless of turbulent Mach number.

An additional length scale correction is also applied based on Bradshaw's relation, $\tau_t/\rho \sim a_1 k$ and the mixing length relation, $\ell = \kappa\, y$. Following the suggestion of Vuong and Coakley,[20] the eddy viscosity is limited to: $\nu_t \leq \sqrt{\tau_t/\rho}\, \ell$. For the two-equation $k-\omega$ models this leads to the following relation:

$$\nu_t = \min(k/\omega, \sqrt{a_1 k}\, \kappa y), \quad (7)$$

And for the two-equation SST model:

$$\nu_t = \min(k/\max(\omega, \Omega F_2/a_1), \sqrt{a_1 k}\, \kappa y) \quad (8)$$

Where, $a_1 = 0.31$, is Bradshaw's constant, $\kappa = 0.41$ is the mixing length constant, Ω is the magnitude of the vorticity vector and F_2 is defined in the Appendix. Except where noted, this length scale correction is applied to all calculations using the $k-\omega$ and SST models.

Transition

Due to the wide range of Reynolds numbers encountered in hypersonic flows, a simple means to specify transition has been implemented into the Ames version of the *GASP* Navier-Stokes code. This transition model is not predictive, but rather allows us to specify, by means of an auxiliary input file, where transition occurs using up to 8 laminar subregions within each grid block. Each laminar subregion, being three-dimensional has six faces. Associated with each face of a laminar subregion is a face transition function, Tr_f, having a specified transition location, x_{tr}, and a specified transition width, Δx_{tr}. Also associated with each face is a logic value, L_{tr}, indicating whether that particular face is active in determining the laminar subregion. In one dimension, this face transition function may be described by:

$$Tr_f = 1/(1+\exp((x_{tr}-x)/\Delta x_{tr})) \quad (9)$$

Where the example face transition function above describes a laminar region for $x < x_{tr}$ and a turbulent region for $x > x_{tr}$.

A composite transition function is then formed from the face transition functions for each active face using analog equivalents of boolean logic functions so that the composite transition function varies smoothly through the grid from a value of near zero when entirely within the laminar subregion to a value of near one when entirely outside the laminar subregion.

For the two-equation models, the turbulent equations are solved over the entire block, regardless of whether there is or there is not an active laminar subregion. However, the composite transition function defined above is introduced into the procedure in two ways, leading to a non-linear effect. First, the production terms, P_k and P_ω, appearing in the two turbulent equations are multiplied by the composite transition function, reducing turbulence levels within each active laminar subregion. Furthermore, the eddy viscosity is also multiplied by this composite transition function, leading to a further reduction in turbulence levels.

For the Baldwin-Lomax, the eddy viscosity is multiplied by the square of the composite transition function, providing a non-linear effect similar to the two-equation models.

The transition function defined above allows for a smooth variation in eddy viscosity through the transition region. The transition function defined above, when squared, is not identical to, but can be made to closely fit the intermittency function of Dhawan and Narasimha.[21]

The location of transition onset and the length of the transition zone must be determined either from experiment, engineering correlations, or by means of a transition prediction technique.

Results

Evaluation and assessment of these several turbulence models are accomplished in the following subsections. A range of cases is considered which is intended to be representative of flows encountered in atmospheric entry hypersonic flows. The first case allows

an initial assessment of the turbulence models as now implemented in the Ames version of *GASP* through a comparison with engineering correlations and results from another code, *CFL3D*. These same turbulence models are then applied to a sequence of hypersonic cold-wall 2D and axisymmetric experiments, followed by a 3D hypersonic cold-wall experiment and finally a Mach 20 flight experiment.

Compressible Engineering Correlations

A comparison of flat plate calculations for the several turbulence models with engineering correlations was the first step in evaluating turbulence model performance. Air as a perfect gas was assumed to be the working fluid. An array of Mach number (0.3, 1.0, 3.0, 10 and 15) and heat transfer (adiabatic and cold-wall with $T_w/T_t = 1/3$) conditions were calculated for each turbulence model. Only the Mach 10 results are presented in this paper, but the discussion refers to the full array. Furthermore, for this portion of the study, to examine code-to-code variation, the widely used *CFL3D* was employed in addition to the Ames-modified *GASP*. By considering results from two codes, confidence is enhanced in the observations reported herein.

A 2-block grid was used for each calculation, with the same grid used for the *CFL3D* and *GASP* calculations. The first block was 21×85 for the region immediately prior to the leading edge of the flat plate, and a 101×85 block was used for the flat plate. Thus, the leading edge interaction was calculated, but the effect of the trailing edge interaction was not included in the present calculations. The grids were optimized for each Mach number and stretched in both streamwise and wall-normal directions. The y^+ value for the first grid point off the wall was typically 1 or less along the entire plate.

Figures 1(a) and 1(b) compare typical C_f vs Re_x results for the Mach 10 adiabatic wall case from *CFL3D* and from the present Ames-modified *GASP*, respectively. Only minimal differences occur in comparing the two codes for each turbulence model.

Also shown in Figs. 1(a) and 1(b) are comparisons of the turbulence results with the the Van Driest II C_f compressibility transformation (see Refs. 22–25) as applied to the C_f vs Re_x correlation of White[26] (solid symbols):

$$C_f = \frac{0.455}{F_c \ln^2(0.06 Re_x F_x)}, \quad (10)$$

and the Van Driest II C_f compressibility transformation as applied to the C_f vs Re_θ correlation of Kármán-Schoenherr[27] (open symbols):

$$\frac{1}{C_f F_c} = 17.08 \log_{10}^2(Re_\theta F_\theta) + 25.11 \log_{10}(Re_\theta F_\theta) + 6.012 \quad (11)$$

Where,

$$F_c = (\frac{T_{aw}}{T_e} - 1)/(\arcsin\alpha + \arcsin\beta)^2, \quad (12)$$

$$F_\theta = \frac{\mu_e}{\mu_w},\ F_x = \frac{F_\theta}{F_c}, \quad (13)$$

$$\alpha = (\frac{T_{aw}}{T_w} + 1 - 2\frac{T_e}{T_w})/\Gamma, \quad (14)$$

$$\beta = (\frac{T_{aw}}{T_w} - 1)/\Gamma, \text{ and} \quad (15)$$

$$\Gamma = ((\frac{T_{aw}}{T_w} + 1)^2 - 4\frac{T_e}{T_w})^{1/2}. \quad (16)$$

T_{aw} is obtained using a turbulent recovery factor of 0.89.

Note that the C_f vs Re_x Kármán-Schoenherr relation plotted in Figures 1(a) and 1(b) (plots of C_f vs Re_x) requires a mapping of Re_θ to Re_x, which is here obtained from the Baldwin-Lomax solution. Use of the Baldwin-Lomax Re_θ to Re_x map for comparison of the Kármán-Schoenherr relation with the other turbulent solutions will, for the fully turbulent cases considered here, lead to no more than a 2% error in the C_f obtained from Kármán-Schoenherr when placed on a C_f vs Re_x plot.

Most of the results from the several turbulence models compare within $\sim$ 10% between the two codes and with the correlations of Eqs. 10 and 11. up to a Mach number of 15, even for the cold-wall cases. The Spalart-Allmaras model (SA in Fig. 1(a)), however, proves to resist transition with increasing Mach number. Other researchers have also indicated this unfavorable delayed transition property of Spalart-Allmaras model for hypersonic flows. Additionally, the $k-\epsilon$ (Chien version) *GASP* results are seen to also have a delayed transition with a significant underprediction of C_f for the Mach 10 and above cases.

Figures 2(a) and 2(b) show the computed skin friction, C_f, and Stanton number, St, for the Mach 10 T_w/T_t cold-wall case, respectively. The engineering correlations for Stanton number are derived from the C_f correlations of White and of Kármán-Schoenherr using the Reynolds analogy factor, $R_f = 2St/C_f$. A value of 1.15 is used for the Reynolds analogy factor based on comments in Ref. 25.

Note that both the SSTc1 and the KW98c turbulence models, which incorporate compressibility corrections, underpredict skin friction and heat transfer for the Mach 10 cases shown here. The high turbulent Mach number present in the near wall region for the Mach 10 boundary layers leads to the imposition of the compressibility correction resulting in the reduction of the turbulence production, whereas this compressibility correction is mainly intended to be active for free shear layers. However, for the SSTc2 turbulence model, the addition of logic to automatically suppress this compressibility correction in the

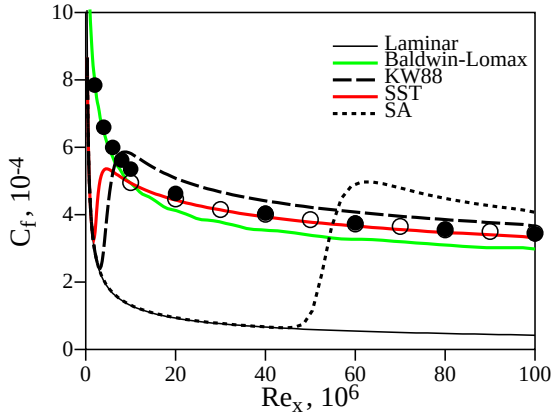

a) *CFL3D* **Calculations**

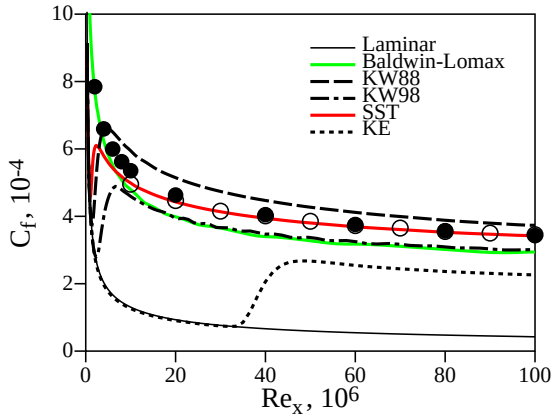

b) *GASP* **Calculations**

Fig. 1 Skin Friction Variation for Mach 10 Adiabatic Flat Plate. Solid symbols–White[26] correlation, open symbols–Kármán-Schoenherr[27] correlation.

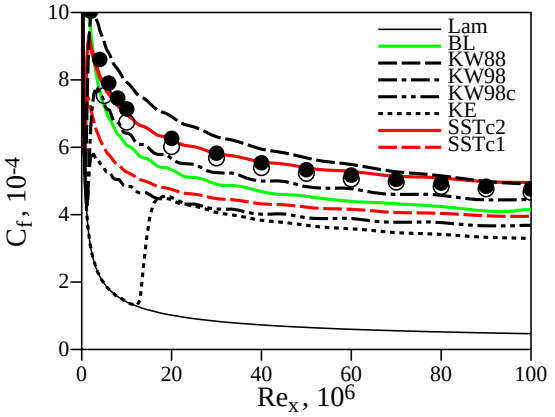

a) **Skin Friction,** *GASP* **Calculations**

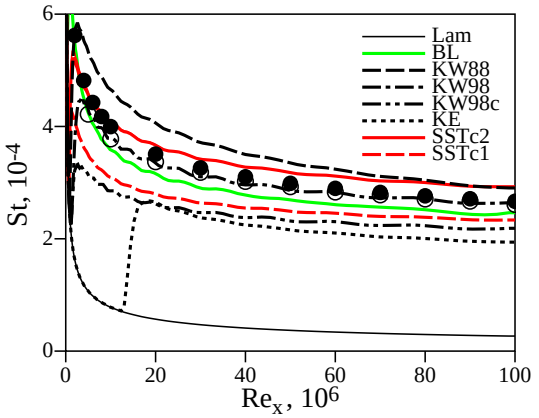

b) **Heat Transfer,** *GASP* **Calculations**

Fig. 2 Skin Friction and Heat Transfer for Mach 10 Cold-Wall ($T_w/T_t = 1/3$) Flat Plate. Solid symbols–White[26] correlation, open symbols–Kármán-Schoenherr[27] correlation.

presence of a wall layer successfully leads to agreement of the SSTc2 model with the standard SST model (not shown) for high Mach number wall-bounded shear layers while retaining the compressibility correction as needed for free shear layers.

An observation, based not only on the Mach 10 adiabatic and cold-wall results shown here, but also from extensive computations of adiabatic and cold-wall flat plate cases up to Mach 15, is that the Baldwin-Lomax, KW98, SST, and SSTc2 models can provide agreement to within $\sim 10\%$ with the compressible forms of standard skin friction and Stanton number heat transfer engineering correlations. The compressibility correction in the KW98c and the SSTc1 turbulence models appears to lead to an underprediction of both skin friction and heat transfer at higher Mach numbers. The KW88 turbulence model shows a tendency to overpredict the skin friction and heat transfer at higher Mach numbers, while the Chien $k-\epsilon$ tends to underpredict the skin friction and heat transfer at higher Mach numbers. Both the Chien $k-\epsilon$ and Spalart-Allmaras turbulence models exhibit an increasing resistance with Mach number to provide transition to fully turbulent flow.

Mach 11.5 Cold-Wall Flat Plate Experiment

The next case considered is the nominal Mach 11.5 cold wall flat plate experiment of Watson.[28,29] This experiment was conducted with Helium as the working fluid. The test model was a cooled-wall sharp-nosed flat plate mounted above the tunnel floor in the freestream of the tunnel and placed at a -4° angle of attack so as to generate a leading edge shock. Important considerations in choosing the experiment of Watson are that the edge Mach number is high and the wall is cold, which are relevant to reentry vehicles. Furthermore, the test model is mounted in the freestream rather than simply a tunnel floor experiment. The latter consideration is important to the thermal boundary layer development and to the relationship of experimental heat transfer to engineering correlations. Extensive measurements were taken, including

heat transfer, skin friction, and pitot tube surveys.

Considerable run-to-run variation in tunnel conditions occurred in the experiment, however, proper normalization of results minimizes this effect. For the present work, the tunnel conditions are assumed to be for a "typical" run and were chosen to be $M_\infty = 18$, $p_t = 13.79$ MPa, $T_t = 311.1K$, $T_\infty = 2.86K$, and a wall temperature of $T_w = 102.6K$, giving $T_w/T_t = 0.33$. Freestream density was specified as $\rho_\infty = 0.0187183\,\mathrm{kg/m^3}$. The freestream unit Reynolds number was $46.1 \times 10^6/\mathrm{m}$. The case considered corresponds to Watson's Table 5, case 43, which is a pitot tube survey. The heat transfer data presented in Stanton number form are from Watson's Table 2, case 23 which is a close match to the conditions calculated.

As the model was at $-4°$ angle of attack, a shock formed at the sharp nose, and the test case is effectively for an edge Mach 11.5 cold-wall flat plate flow. Nominal edge conditions, based on oblique shock relations, are $\rho_e = 0.0453\ \mathrm{kg/m^3}$, $U_e = 1770$ m/s, and $T_{aw} = 277K$ using a turbulent recovery factor of 0.89.

A 109×85 (streamwise $\times$ wall-normal) grid was used for the Navier-Stokes calculations. The leading edge of the flat plate is located at the 9th streamwise grid point, thereby capturing the shock. The grid is stretched in the wall-normal direction with the first grid point located 4 μm away from the wall for stations near the laminar leading edge gradually increasing to 20 μm within the turbulent regions. The Van Leer flux formulation was used for the streamwise flux and the Roe flux formulation was used for the wall-normal flux.

Figure 3(b) shows a comparison of experimental heat transfer data and results from *GASP* solver utilizing several turbulence models. The results are plotted in the normalized form of Stanton number based on edge values vs $Re_{x,\infty}$ (using the freestream unit Reynolds number from above). Transition to turbulence plays a considerable role in this experiment. Transition is specified in the solutions at the experimental location of 0.5 m ($Re_{x,tr} = 23 \times 10^6$). The high Reynolds number for transition is a characteristic of high Mach number flows and is related in part to the low freestream dynamic viscosity associated with the low freestream temperature. The variation of heat transfer through the transition region appears well represented by the current transition modeling as implemented for the several turbulence models. The Baldwin-Lomax, the SSTc2, and the KW98 turbulence models predict the wall heat transfer levels for the turbulent region quite well, all within experimental error. The SST model (not shown) gives nearly identical results to the SSTc2 model. The $k-\epsilon$ model significantly underpredicts wall heat transfer, while the KW88 model over predicts by a considerable margin.

Figure 3(a) shows wall skin friction measurements and computational results for this flow. The data are

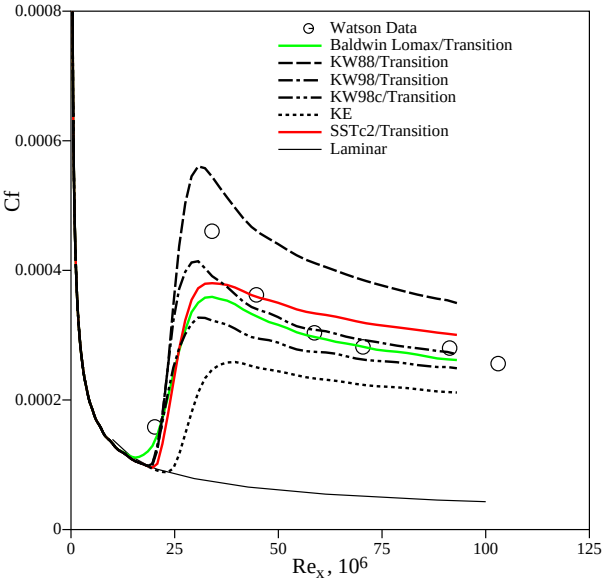

a) Skin Friction

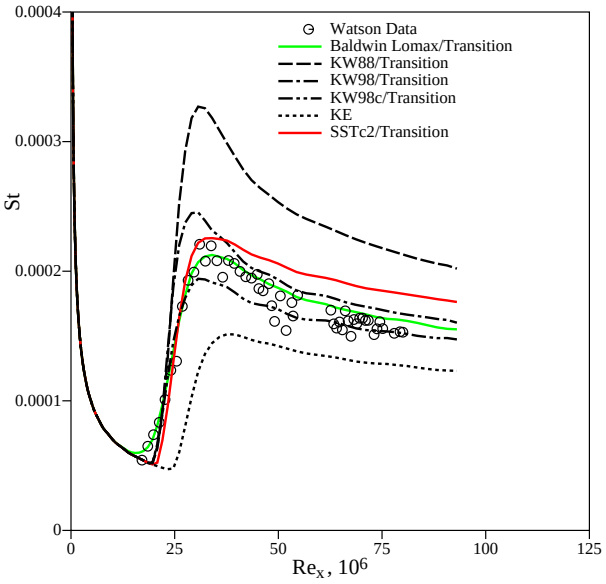

b) Heat Transfer

Fig. 3 Skin Friction and Heat Transfer for Watson[28] Mach 11.5 Experiment, $T_w/T_t = 1/3$

from Fig. 15 of Watson.[28] The wall skin friction in Fig. 3(a) is based on edge conditions, $C_f = 2\tau_w/(\rho_e U_e^2)$. The wall skin friction and Stanton number are related surface properties, but are actually acquired by independent instruments. Prior to transition, all calculations predict laminar wall skin friction in agreement with laminar theory[30] (see Fig. 15 of Ref. 28). At transition there appears to be a significant overshoot in wall skin friction measurements which is not evident in any of the computations. However, after transition the measured wall skin friction falls to a plateau which slowly decreases for the remainder of the turbulence region measured. As with the heat transfer results,

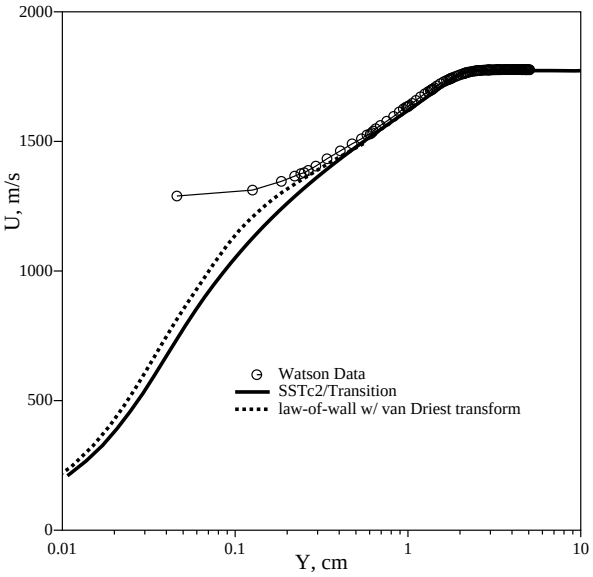

Fig. 4 Velocity Profile, Compressible law-of-wall. Watson Mach 11.5, $T_w/T_t = 1/3$ Experiment of Watson[29] (Table 5, Case 43), $Re_x = 88 \cdot 10^6$.

the KW88 model is seen to overpredict the turbulent skin friction level, while the Chien $k-\epsilon$ model significantly underpredicts skin friction. The agreement of the Baldwin-Lomax, SSTc2 and the KW98 turbulence models with both the skin friction and heat transfer measurements for this cold-wall, high Mach number turbulent flow adds considerable confidence to use of these models for "acreage" heat transfer estimates in atmospheric entry environments.

Figure 4 depicts measured velocity profiles (derived from pitot pressure measurements) along with the compressible law of the wall (labeled Van Driest transformation) and SSTc2 calculations for the same location. The Van Driest velocity transformation shown in Fig. 4 makes use of the analytical transformation of a tabulated form of the incompressible law-of-wall velocity profile of Coles[31] to account for the compressible cold-wall conditions of the present case. Excellent agreement is achieved, except for probe interference effects close to the wall.

Mach 7.05 Compression Corner Experiment

Next examined is the cold wall ($T_w/T_{aw} = 0.35$) Mach 7.05 compression corner of Kussoy and Horstman.[32] Figure 5 depicts the experimental configuration. This data is also compiled in the Hypersonic Shock/Boundary-Layer Interaction Database of Settles and Dodson, described in Ref. 33 and presented in detail in Ref. 34. This test was conducted in the NASA Ames 3.5 foot Hypersonic wind tunnel. The freestream density was $\rho_\infty = 0.0252$ kg/m^3, with $p_\infty = 576$ Pascal, and $T_\infty = 81.2K$. Wall temperature was $T_w = 311K$. The total pressure was $p_t = 25$ atm, and total temperature was $T_t = 888K$. Conical flares

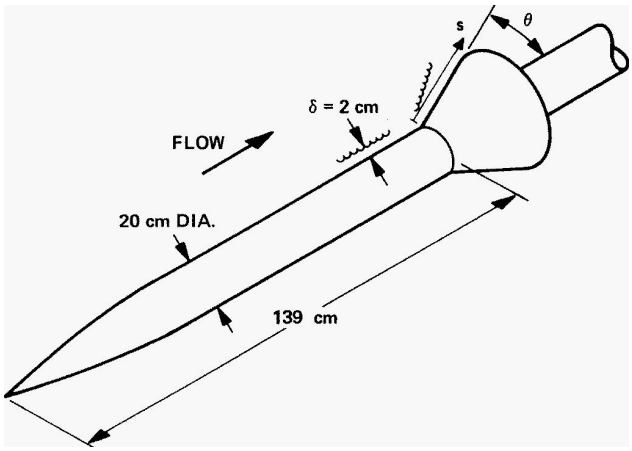

Fig. 5 Mach 7.05 Compression Corner Experiment of Kussoy and Horstman.[32]

of 20°, 30°, 32.5° and 35° half-angle were mounted at the 1.39 m x-station of a 10 cm radius cylinder with its axis aligned with the freestream. These several cone angles provided a range of incipient separation to fully separated cases. The 35° axisymmetric flare is of primary interest in this current paper as several authors have also calculated this case, (in particular, Coakley and Huang[35]). This experiment is of interest as compression corner flows are related to the deployment of control surfaces on entry vehicles.

For this experiment, a 2 cm thick turbulent axisymmetric boundary layer developed on the cylinder, with $C_{f0} = 0.00122$, which then encountered the conical compression corner. The length of the initial cylinder flow was adjusted for each turbulence model case so as to match the initial C_f value. Note this procedure does not, in general, result in a match in initial heat transfer.

The Navier-Stokes calculations were conducted with the VL2R flux option on a 149×93 (streamwise $\times$ wall-normal) axisymmetric grid. A y^+ value of 0.25 was typical for the first grid point off the wall.

In Figs. 6(a) and 6(b), the wall pressure and heat transfer results for Navier-Stokes computations using the Baldwin-Lomax, SSTc2, KW98 and KW88 turbulence models are compared with the experimental measurements for the 35° fully separated case. Computational results from Coakley and Huang[35] for the 1988 version of the $k-\omega$ model are presented as well. Their length-scale modified version is shown since this corresponds closely to the present *GASP* KW88 implementation. Note that Kussoy and Horstman's heat transfer data and Coakley and Huang's computational results were presented in Refs. 32 and 35 in the form of $q/q_{0,\text{exp}}$ vs s, where s is the arc length along the cylinder and the 35° compression ramp. The heat transfer just upstream of the compression corner is given by Ref. 32 as $q_{0,\text{exp}} = 0.93$W/cm^2. The plots in Fig. 6(b) is in terms of q, the wall heat transfer rate. Furthermore, the plots in Figs. 6(a) and 6(b) are in terms

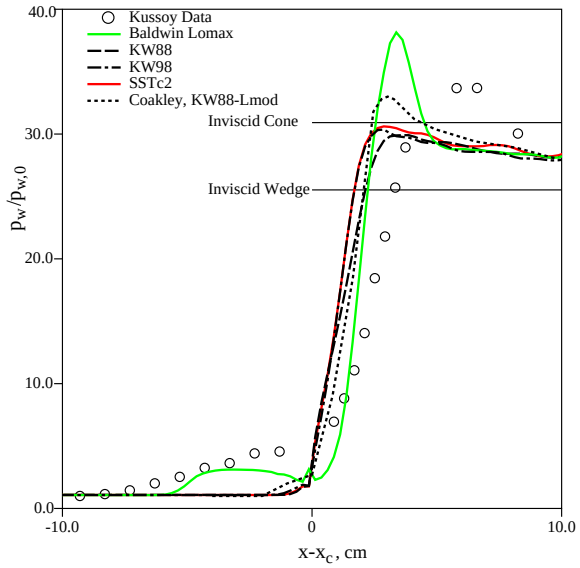

a) Wall Pressure

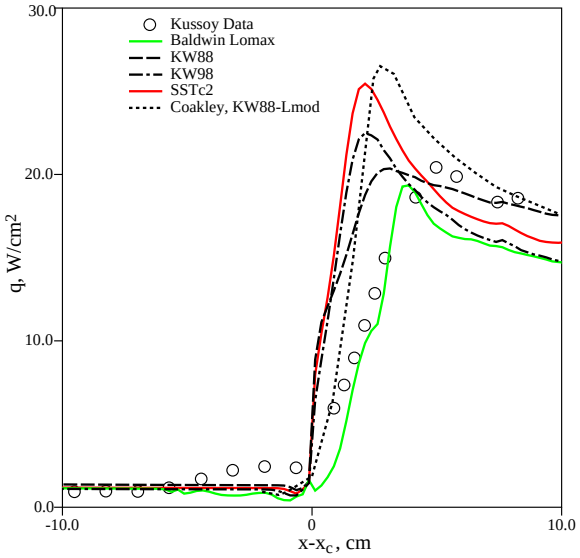

b) Heat Transfer

Fig. 6 Wall Pressure and Heat Transfer for Mach 7.05, $T_w/T_{aw} = 0.35$ Compression Corner Experiment of Kussoy and Horstman.[32]

of $x - x_c$, the axial distance along the cylinder from the compression corner, rather than s, the arc length along the surface.

Also shown on the pressure plot are the pressure levels derived for a inviscid flow over a 35° cone and a 35° wedge for the same freestream conditions. From the wall pressure results, the Baldwin-Lomax is seen to somewhat underpredict the spatial extent of the separated zone on the cylinder before the corner, while the two-equation turbulence models are quite resistant to separation, with only a very small separation bubble. Furthermore, for the separated region before the corner, all models exhibit a tendency for the heat transfer to actually decrease in the separation region on the cylinder whereas the experiment indicates a rise in heat transfer.

Once the corner is encountered, the experimental pressure rises rapidly and overshoots the inviscid cone pressure level before decreasing to a level partway between the inviscid cone and inviscid wedge pressure levels as might be anticipated. The Baldwin-Lomax pressure results also indicate a pressure overshoot but with the subsequent pressure plateau in good agreement with experiment. All of the two-equation models shown avoid significant pressure overshoot and merely rise to a pressure plateau, again with the plateau level in good agreement with experiment. The location of the pressure overshoot may be considered to be an indication of reattachment. As such, reattachment for all of the turbulent calculations considered here is located only 1/2 of the distance along the cone relative to the experimental reattachment location.

The heat transfer level for the Baldwin-Lomax turbulence model for the region past the corner shows the same shape as the experimental curve, but with a roughly 10% underprediction. The SST and KW98 turbulence models both show the same general trend in heat transfer past the corner, with an overshoot of $10 - 20\%$ followed by a decrease to about 10% below the experiment. The KW88 model shows good agreement as to heat transfer levels past the compression corner. However, all of the two-equation models provide a significantly smaller separation region than either the Baldwin-Lomax or the experimental results.

The $k - \omega$ computations of Coakley and Huang shown in the pressure plot indicate a somewhat larger separation region than do the *GASP* KW88 results, although still significantly smaller than measured in the experiment. This difference in extent of the separation bubble between Coakley and Huang and the present $k - \omega$ calculations appears to impact the overshoot in heat transfer level at reattachment as well. Past reattachment, heat transfer levels obtained with the Coakley and Huang 1998 $k - \omega$ implementation and the *GASP* KW88 implementation achieve agreement with experiment to within $\sim 8\%$. These two codes are considerably different in many details and such differences should be anticipated, particularly for strong interactions such as shock-separated flows.

The $k - \epsilon$ results for this case (not shown) indicate an significant and unacceptable overshoot in heat transfer for the separated region, see also Coakley and Huang.[35]

Improvements on the turbulence models considered here would be desirable for a more detailed agreement for separated compression corners, but for thermal protection design purposes, the agreement may be considered adequate provided a suitable margin of error is used.

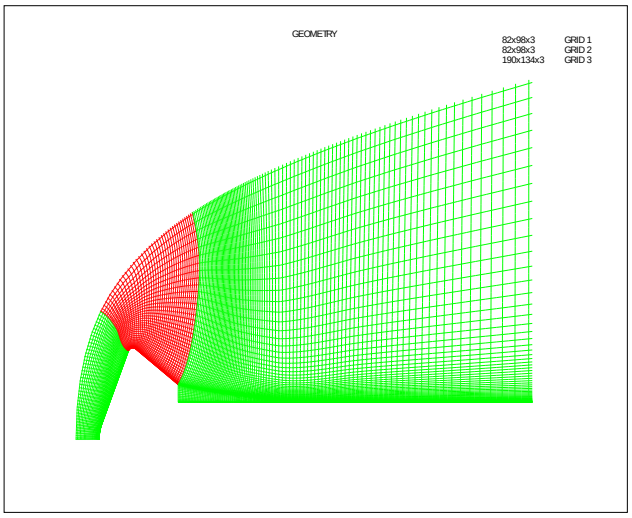

Fig. 7 Three Block Grid for Mach 10, 70° Sphere-Cone of Hollis.[36] Every 2nd grid line shown.

Mach 9.8, 70° Sphere-Cone Experiment

Many of the planetary missions to Mars, both past and planned, are based on a 70° sphere-cone forebody geometry, with various aftbody configurations. Specification of thermal protection for vehicles being planned depends on the accuracy of and confidence in heat transfer predictions for such geometries.

The performance of various turbulence models as they relate to the aftbody region of hypersonic planetary entry vehicles is addressed by considering the heat transfer experimental results of Hollis[36] and Hollis and Perkins.[37] In this experiment, a 70° sphere-cone with a 40° cone-frustum aftbody is mounted on a sting and placed in a nominal Mach 10 flow. This configuration is quite similar but not identical to the Mars Pathfinder spacecraft (49.5° cone-frustum aftbody) and is referred to by Hollis as case MP1. The experiments were conducted in both a wind tunnel and a high-enthalpy shock tunnel and with several different gases, including air and CO_2. Emphasis for this experiment was on heat transfer measurement; no wall pressures were obtained. Laminar Navier-Stokes computations on a 125×90 grid were also presented by Hollis.

The experimental test conditions for the case computed here were representative of Hollis test 293, run 6 and test 307, run 22, which are for air. The freestream conditions for the Navier-Stokes calculations were $M_\infty = 9.795$, $T_\infty = 52.45K$ and mixture density of $\rho_\infty = 0.00868$ kg/m^3. Cold-wall conditions prevailed with a wall temperature of $T_w = 300K$. With the base radius of $R_b = 2.54$ cm, the Reynolds number based on diameter was 92,000. This Reynolds number was too low for transition to occur on the forebody, even with tripping. Such a low Reynolds number, relative to anticipated Mars entry conditions, is a limitation common to currently available experimental data. Due to the presence of a sting rather

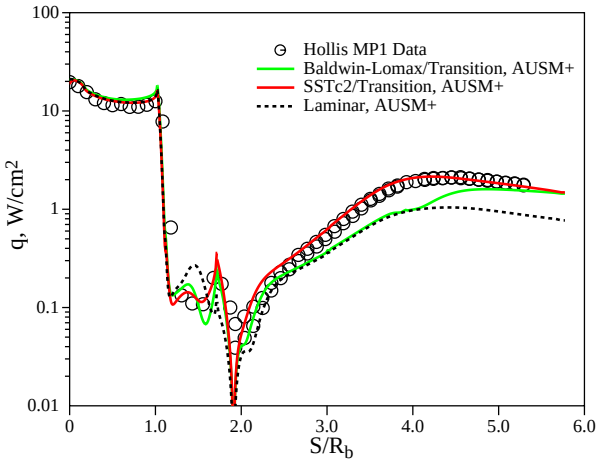

a) Heat Transfer

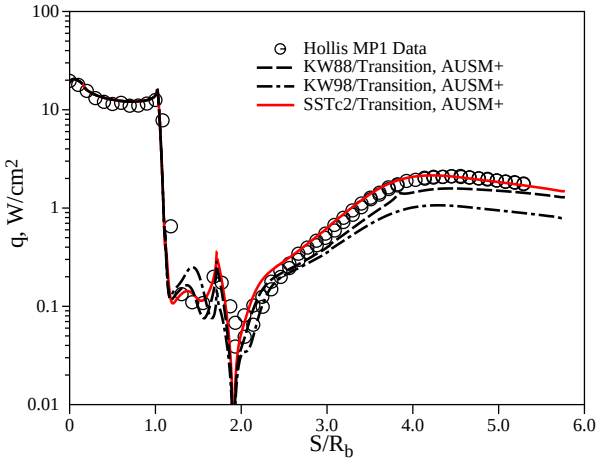

b) Heat Transfer for $k-\omega$ turbulence models.

Fig. 8 Heat Transfer for Mach 10, 70° Sphere-Cone of Hollis.[36]

than an isolated wake, however, transition to turbulence does appear to occur on the sting section, which is also instrumented.

A 3-block grid (see Fig. 7) was used with a 81×97 grid for the forebody, a 81×97 grid for the aftbody and a 189×133 grid for the wake/sting flow regions. The flow was axisymmetric.

Figures 8(a) and 8(b) compare the heat transfer result obtained for different turbulence models to the experimental results. The flow over the sphere-cone forebody is laminar, with transition specified as occurring past the shoulder and turbulent flow for the aftbody and sting. Agreement is excellent for the forebody as might be expected for all calculations. Along the aftbody and onto the sting, the SSTc2 model provides excellent agreement with experiment. The SSTc2 model calculations provide the only predictions that agree with the experiment to within 10%. Further, the SSTc2 model captures the detailed variation of the heat transfer on the aftbody frustum. Both

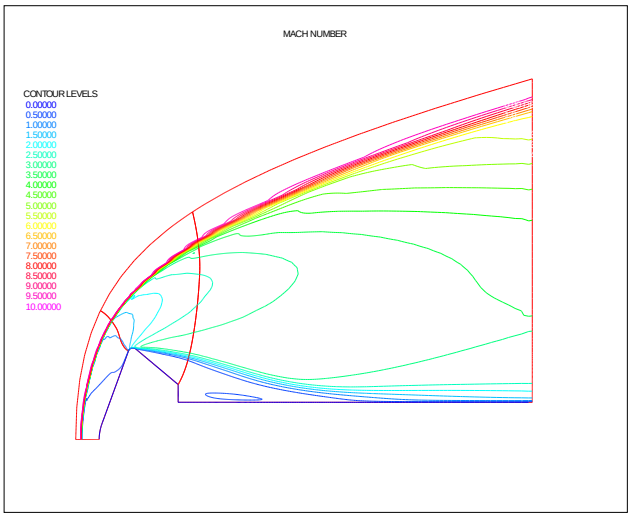

a) Mach Number

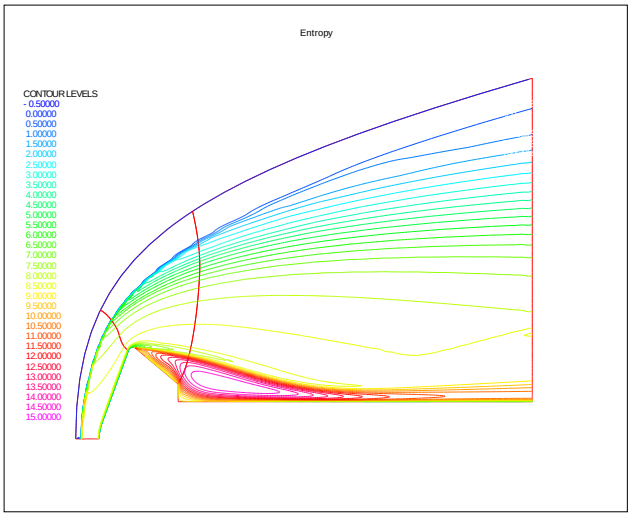

b) Entropy

Fig. 9 SST Turbulence Model Solution Mean Flow Contours for Mach 10, 70° Sphere-Cone of Hollis.[36]

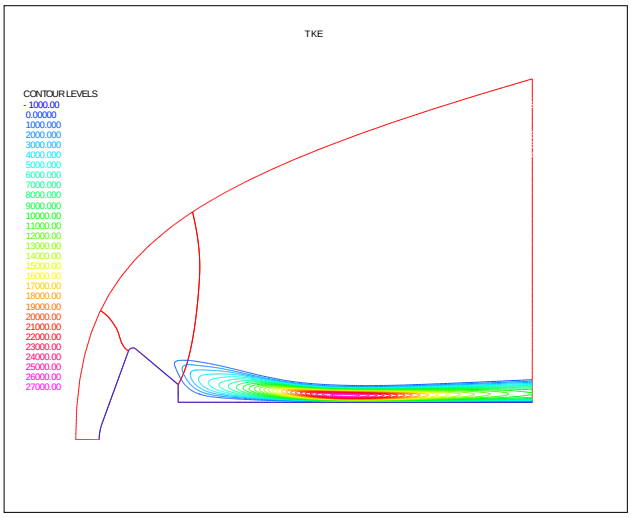

a) Turbulent Kinetic Energy, k

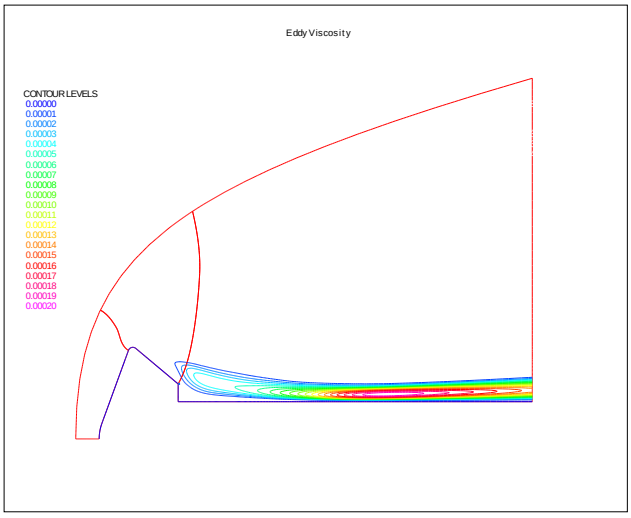

b) Turbulent Eddy Viscosity, ν_t

Fig. 10 SST Turbulence Model Solution Turbulence Contours for Mach 10, 70° Sphere-Cone of Hollis.[36]

the Baldwin-Lomax and KW98 models severely underpredict the heat transfer on the sting by 50%, while the KW88 calculation underpredicts the experiment by roughly 20%.

Contours of Mach number, entropy, turbulent kinetic energy and eddy viscosity from the SSTc2 Navier-Stokes calculations are presented in Figs. 9(a), 9(b), 10(a) and 10(b), respectively, for the Hollis MP1 case. Flow behind the shock, but on the forebody is subsonic with the sonic line occurring just before the shoulder. A strong expansion fan around the shoulder is followed by large-scale separation over the aftbody. A lip shock originating from the shoulder can be observed in the entropy contour. The recompression shock can be seen in the aft portion of the sting beginning at about attachment point on the sting. The eddy viscosity and turbulent kinetic energy contours are quite similar in their development, as might be expected. Significant turbulence is not predicted to occur until just before the end of the aftbody frustum. Although, transition is specified in these calculations at the shoulder, the expansion fan suppresses initial development of the turbulence field.

Mach 7.4 Ames All-Body Experiment

The Ames All-Body experiment of Lockman et al.[38] provides a well-documented, hypersonic 3D test case suitable for the present turbulence model validation. The configuration is a generic lifting body intended for hypersonic cruise and is based on analytical studies. The experiment was conducted in the Ames 3.5 foot Hypersonic wind tunnel.

The Ames All-Body test model is shown in Fig. 11. The model was $L = 0.9144$ m (3 feet) in length and consisted of a 75° sweepback sharp-nosed delta planform. The forebody was an elliptic cone with a major-

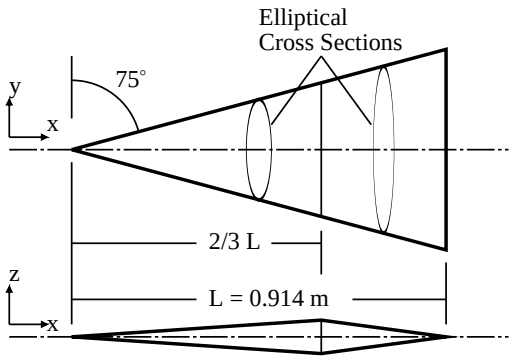

Fig. 11 Ames All-Body Mach 7.4 Experiment of Lockman et al.[38]

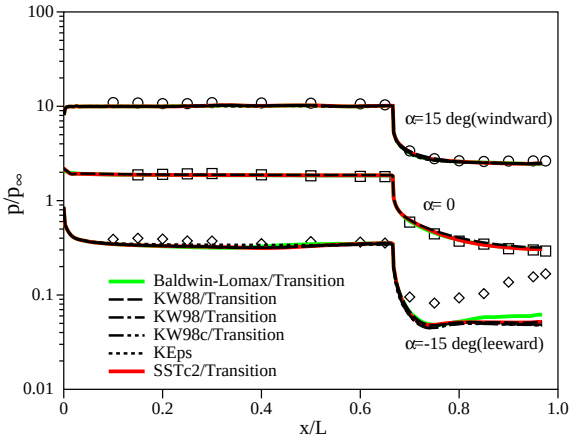

Fig. 12 Centerline Wall Pressures for Ames All-Body Mach 7.4 Experiment of Lockman et al.[38]

to-minor axis ratio of $a : b = 4$, while the aftbody had elliptic cross-sections tapering to a straight-line trailing edge.

The test conditions for the Ames All-Body experimental cases examined in this paper are $M_\infty = 7.4$ and $Re_L = 15 \times 10^6$. The freestream total temperature, T_t, was $722K$ and the model wall temperature, T_w, was $300K$ for these experiments. The tests were for cold-wall conditions, $h_w/H_\infty = 0.4$. The working fluid was air. Due to the low freestream temperature, $T_\infty = 62K$, the equation of Keyes[39] is used for evaluating dynamic viscosity in reporting the Reynolds number and for the Navier-Stokes computations.

Measurements for this experiment included heat transfer and wall pressure, both along the centerline and spanwise. Pitot probe surveys were also conducted on the aftbody along the centerline. The model was tested at angles of attack of 0°, 5°, 10° and 15°. Measurements were made, on different runs, on both the leeward and windward sides of the model.

Prior computations of this experiment include (1) Parabolized Navier-Stokes (PNS) calculations reported by Lockman et al.[38] using the UPS code developed by Lawrence et al.,[40] and (2) Navier-Stokes calculations reported by Prabhu et al.[41] using an earlier version of the *GASP* code. In these prior computations, Baldwin-Lomax was the only turbulence model used.

Computations were accomplished for the present paper for the 0° and the 15° angle of attack cases. The grids for these two cases were the same single-block $111 \times 101 \times 64$ (streamwise × spanwise × wall-normal) grids used by Prabhu et al.[41] The y^+ value for the first node from the wall was never greater than 0.1 for all cases considered. For the 0° angle of attack case, the flow was assumed fully turbulent. Solutions were obtained for the Baldwin-Lomax, SSTc2 and KW88 turbulence models. For the 15° angle of attack case, transition to turbulence was specified on the forebody at $x = 0.235$ m, for both the windward and leeward sides. Solutions using the Baldwin-Lomax, SST, SSTc1, SSTc2, KW88, KW98, KW98c and $k - \epsilon$ turbulence models were all obtained using the mixed VL2R (Van Leer/Roe) flux option, except where noted. Additional solutions for the Baldwin-Lomax and the SSTc2 turbulence models were also obtained using the VL3 (Van Leer formulation in all 3 coordinate directions) and AUSM$^+$ (all 3 coordinate directions) flux options. Additional fully turbulent solutions for the 15° angle of attack case were accomplished for the SSTc2 and Baldwin-Lomax turbulent models.

In Figure 12, centerline wall pressure for both the experiment and computations are shown for the 15° windward side, the 15° leeward side and the 0° test cases. The computational results shown include the Baldwin-Lomax, SSTc2, KW88, KW98, KW98c turbulence models (specified transition) and the $k - \epsilon$ turbulence model (fully turbulent) using the mixed VL2R flux option.

Overall excellent agreement exists among the experiments and the several computations for the wall pressures using the different turbulence models. Note that for the 15° leeward aftbody ($x/L > 2/3$), the experimental pressures are quite low and difficult to measure.

For the 15° windward wall pressures on the forebody (for $x < 2/3L$), the computations using the various turbulence models agree among themselves quite well, but the experimental wall pressures are about 10% higher for the forebody. This result was also observed in the earlier computations of Lawrence (in Lockman et al.[38]) and of Prabhu et al.[41] In these earlier computations, excellent agreement with windward pressures

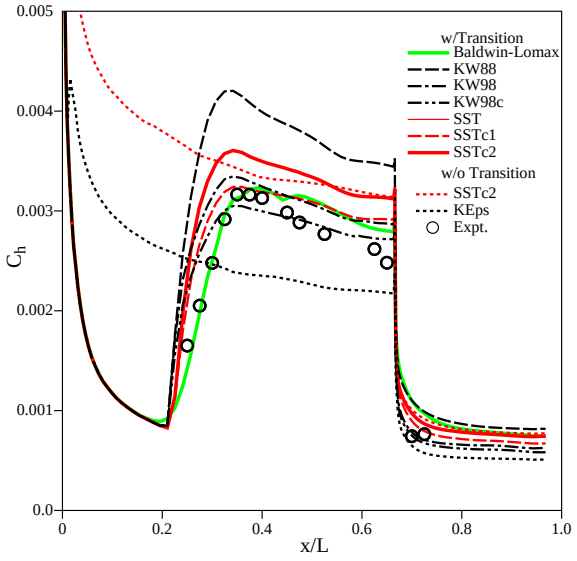

a) 15°, **Windward Side**

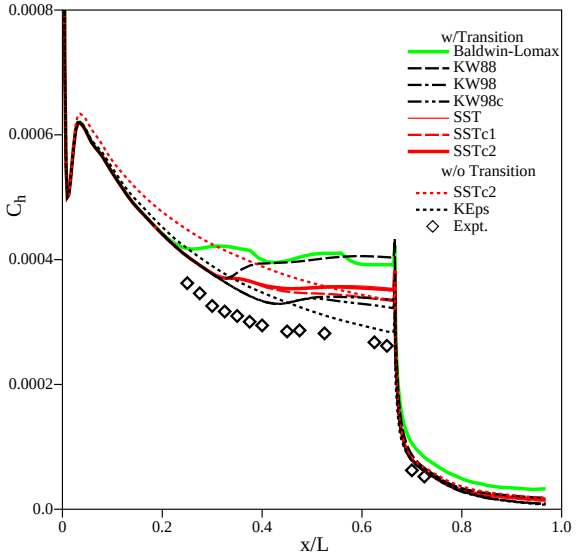

b) 15°, **Leeward Side**

Fig. 13 Centerline Heat Transfer for $\alpha = 15°$, Mach 7.4 Ames All-Body Expt of Lockman et al.[38]

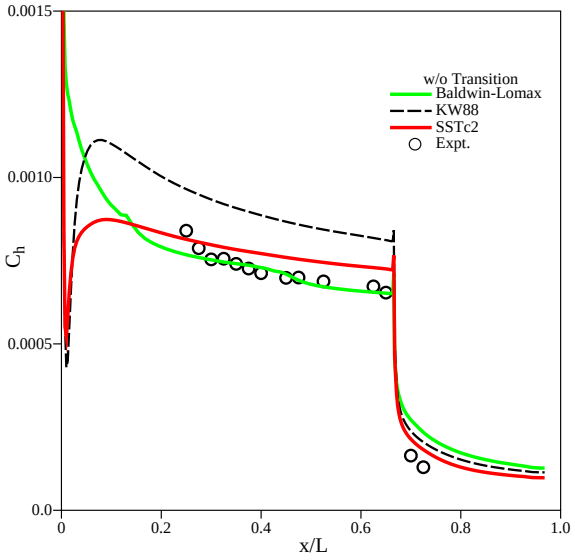

Fig. 14 Centerline Heat Transfer for $\alpha = 0°$, Mach 7.4 Ames All-Body Expt of Lockman et al.[38]

were obtained for the entire forebody at lower angles of attack (5° and 10° not computed in the present paper). Lawrence also obtained the 10% discrepancy for the 15° windward forebody pressure similar to the present calculations.

For the 0° wall pressures, the computational and experimental wall pressures give excellent agreement over the entire model.

In Figs. 13(a), 13(b), and 14, the centerline heat transfer is presented in normalized form, $C_h = q_w/\rho_\infty U_\infty (H_\infty - h_w)$, for both the experiment and computations for the windward and the leeward sides of the 15° and the 0° angle of attack test cases. For the heat transfer, unlike the wall pressure results above, noticeable differences occur between the computational results for the various turbulence models.

For the 15° windward side (Figure 13(a)), the Baldwin-Lomax and KW98 turbulent computational results agree quite well with the experimental results. The SST and SSTc2 turbulent computational results are essentially identical and overpredict heat transfer by about 15% relative to the experiment. The KW98c turbulent computational results underpredict heat transfer slightly relative to the experiment. The KW88 turbulence model, however, overpredicts heat transfer on the windward side by an unacceptable 30%. The $k - \epsilon$ turbulent model significantly underpredicts the heat transfer on the windward side by 25%.

While the pressure distributions appear unaffected by the choice of locating transition at the leading edge or at $x = 0.235$ m, the heat transfer distributions on the 15° windward side are strongly affected by this choice. Note that with transition specified for the Baldwin-Lomax model, the heat transfer rises from the laminar level smoothly to near the fully turbulent level. The present form of introducing transition to the Baldwin-Lomax model appears to match the observed transition curve quite well. The two-equation models, have a sudden jump in heat transfer level at a the beginning of transition followed by a more gradual rise in heat transfer.

For the 15° leeward side (Fig. 13(b)), the experimental heat transfer indicates that transition may not have occurred. As a consequence, past the specified transition point, but on the forebody, all of the turbulence models overpredict the heat transfer, except the $k - \epsilon$ model which appears to entirely resist tran-

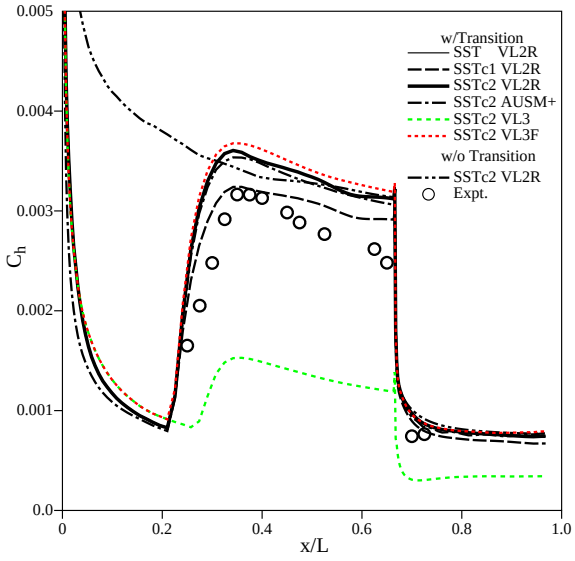

Fig. 15 SST turbulence model option effect on Centerline Heat Transfer for $\alpha = 15°$ windward side, Mach 7.4 Ames All-Body Expt of Lockman et al.[38]

sition. Actually, the Baldwin-Lomax and the KW88 models appear to provide the worst heat transfer prediction on the leeward forebody. This overprediction by the Baldwin-Lomax model on the leeward side may be related to a difficulty of the model to determine the eddy viscosity levels in the presence of the complex vortical flow occurring on the leeward side of this lifting body. The SSTc2 and KW98 models do somewhat overpredict heat transfer on the leeward forebody past transition.

Only the Baldwin-Lomax, KW88 and SSTc2 models were used to compute the 0° angle of attack case. Figure 14 shows these heat transfer results compared with experiment. These were fully turbulent computations. Consistent with prior observations, the Baldwin-Lomax model appears to accurately predict the heat transfer levels on the centerline, with the SSTc2 model providing an overprediction by about 10%. The KW88 turbulence model, however, provides the worst overprediction of about 20% relative to experiment.

In Fig. 15, the heat transfer results for the 15° windward side are compared between several of the available computational options for the SST turbulence model. For this figure, results for the VL2R, AUSM$^+$ and VL3 flux options are shown. The AUSM$^+$ and the VL2R flux options give nearly the same heat transfer results, which is an overprediction, while the VL3 option significantly underpredicts heat transfer when used with the SSTc2 turbulence model. This sensitivity of heat transfer to the flux option appears also with the several $k-\omega$ turbulence models, but not the Baldwin-Lomax model.

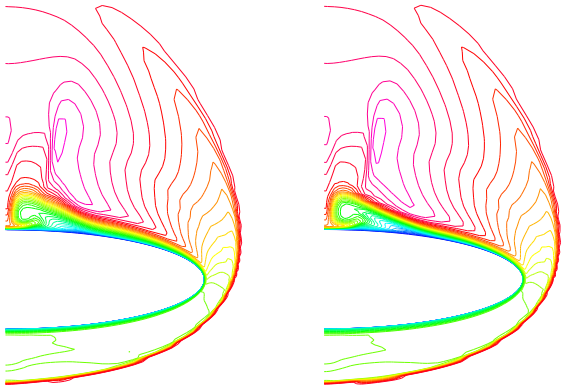

a) Baldwin-Lomax **b) SSTc2**

Fig. 16 Mach Contours for $\alpha = 15°$, Mach 7.4 Ames All-Body Expt of Lockman et al.[38]

A modification to the Van Leer flux option was implemented where the Van Leer split flux continues to be used for the mean flow equations, but the full or unsplit upwind flux is used for the turbulence equations. Since the wave speed associated with the convective terms in the two turbulence equations is simply the local fluid velocity, the use of a split flux with the turbulence equations should not be required. This option of VL3 for the mean flow equations combined with the full unsplit flux for the turbulence equations is referred to in Fig. 15 as VL3F. The heat transfer results for the VL3F option proved to be comparable to the VL2R and the AUSM$^+$ flux options, thereby resolving the issue.

Figure 16 shows Mach number contours for the 15° angle of attack case computed for a plane normal to the body axis located on the forebody at $x/L = 0.6$. This plane is located just before the forebody/aftbody junction. Results from both Baldwin-Lomax and SSTc2 computations are presented and appear quite similar. The flow structure on the windward surface (lower surface in the figure) is seen to be relatively simple, consisting of a bow shock, an outer inviscid flow and a thin boundary layer close to the wall. The leeward (upper) surface, however, contains considerable flow structure. Observed on the leeward side is a cross-flow shock with a primary cross-flow separation outboard of this shock, reattachment and a secondary cross-flow separation embedded within the primary cross-flow separation. These same structures were observed in the PNS calculations presented in the paper of Lockman et al. (see Fig. 7 of Ref. 38). The flowfield structures observed in these computational contours appear to be consistent with surface oil flow visualization studies presented by Lockman et al. (see Fig. 5 of Ref. 38).

The existence of these complex vortical and separation flow structures on the leeward side of lifting

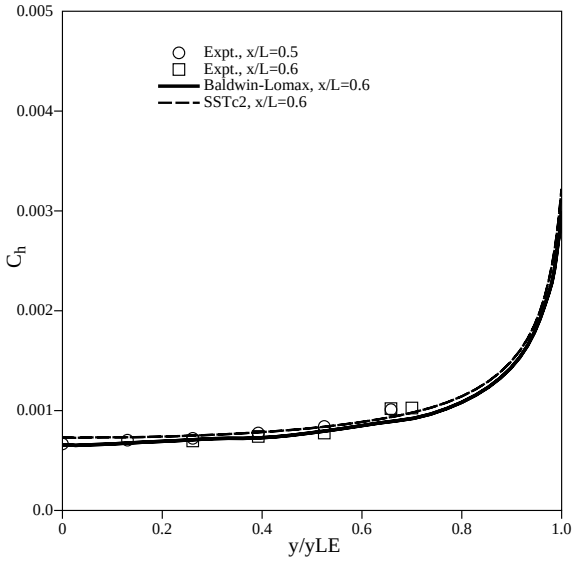

a) $\alpha = 0°$ **Case**

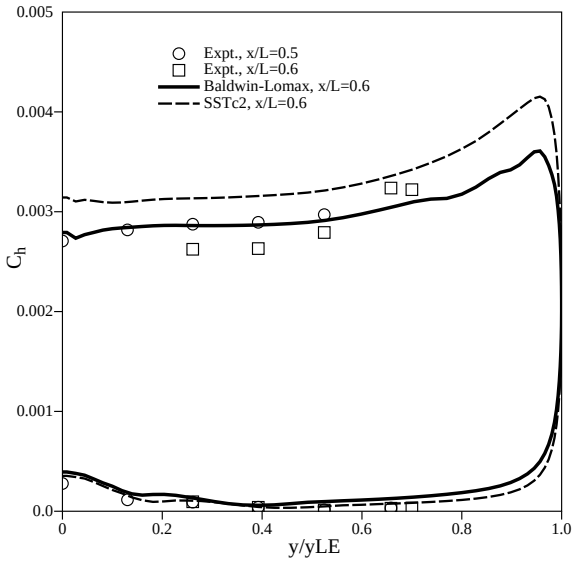

b) $\alpha = 15°$ **Case**

Fig. 17 Spanwise Heat Transfer for Mach 7.4 Ames All-Body Expt of Lockman et al.[38]

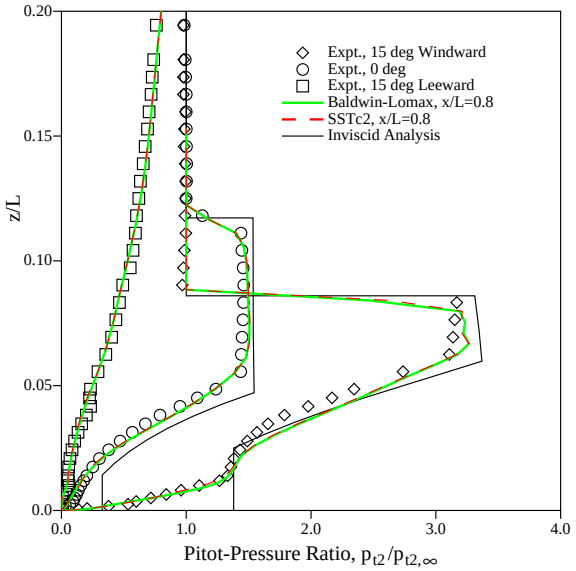

a) Pitot Profile

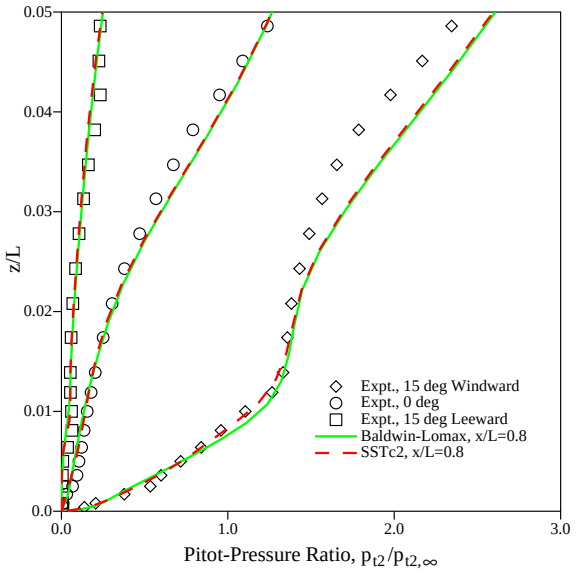

b) Near-Wall Pitot Profile

Fig. 18 Pitot Profiles for Mach 7.4 Ames All-Body Expt of Lockman et al.[38]

bodies likely provides a challenge to the Baldwin-Lomax turbulence model to algebraically specify the eddy viscosity from the velocity profiles near the wall. Resulting is the difficulty observed in Fig. 13(b) where the Baldwin-Lomax turbulence model overpredicts the heat transfer on the leeward forebody by about 30%, while the SSTc2 model overpredicts heat transfer by a lesser amount.

Figures 17(a) and 17(b) show spanwise heat transfer results for the Baldwin-Lomax and SSTc2 turbulence models as compared with the experiment for the $\alpha = 0$ and 15° angle of attack cases, respectively. The computational results are for $x/L = 0.6$, a location on the forebody just before the forebody/aftbody juncture. The experimental distributions for $x/L = 0.5$ and 0.6 are seen to agree along conical rays of y/y_{LE}. Note that y is the spanwise ordinate, and y_{LE} $(=x \tan 15°$) is the spanwise y value of the leading edge for the station considered. The general trends of both the Baldwin-Lomax and SSTc2 turbulent results agree quite well with experiments. The heat transfer increases with spanwise location from the windward centerline towards a maximum value near the leading edge. Further, for the leeward side of the 15° angle of attack case a very low level of heat transfer is observed except for a slight increase in heat transfer close

to the centerline. Both turbulence models describe this leeside heat transfer increase. Furthermore, the level of heat transfer for the Baldwin-Lomax turbulent results is in excellent agreement with experiment for both test cases. The SSTc2 turbulent heat transfer levels, however, appear to be about 10% high relative to the experimental results on the windward side for the 15° angle of attack test case.

Experimental pitot pressure surveys were also obtained by Lockman et al. at $x/L = 0.8$, a location on the aftbody centerline. Figures 18(a) and 18(b) show these measurements as well as the results from the Baldwin-Lomax and SSTc2 turbulence model computations. Evident in these figures are the boundary layer, shock and expansion fan structures for the windward and leeward sides of the 15° test case and for the 0° test case. The computations appear to capture these structures quite well. The inviscid shock and expansion structures do not seem to be noticeably influenced by the choice of turbulence model, as might be expected. Figure 18(b) shows expanded near-wall profiles within the boundary layer where only slight differences are observed between the computed results for the two turbulence models and the experimental results.

Mach 20 ReEntry F Flight Experiment

The REENTRY F flight experiment was conducted on April 27, 1968 and is reported by Carter et al.,[42] and Wright and Zoby.[43] For this experiment, a spacecraft was launched to outside the Earth's atmosphere with the first two stages of a three-stage Scout launch vehicle. The spacecraft was accelerated back into the atmosphere using the final stage rocket. The spacecraft was stabilized by inducing a roll rate of 62 revolutions per minute about the body axis (approximately 1 revolution every 1450 body lengths of travel). The spacecraft entered the Earth's atmosphere on a ballistic trajectory and maintained a nearly constant Mach 20 and zero angle-of-attack for most of its flight back into the atmosphere. Extensive heat transfer and pressure data were obtained via telemetry as the vehicle descended from above 36,576 m (120,000 feet) to below 18,288 m (60,000 feet) altitude. The data at various altitudes provide a variation in Reynolds number. Thus at higher altitude, the flow is laminar while at lower altitudes laminar/transition/turbulent conditions are seen. Vehicle breakup occurred at about 12,192 m (40,000 feet) altitude.

The spacecraft was a 5° half-angle cone 3.962 m long, having a base diameter of 0.693 m and with an initial nose tip radius of 0.254 cm. The skin of the cone was made of 1.52 cm thick beryllium and the nose tip was made of graphite. The nose tip radius increased gradually due to ablation during reentry.

Transition to turbulence first occurred towards the aft end of the cone at an altitude slightly above 30,480 m (100,000 feet). The transition location then moved forward on the cone as the vehicle descended through the atmosphere. At an altitude of 24,384 m (80,000 feet), the transition front had moved to a streamwise location roughly 70% the length of the vehicle.

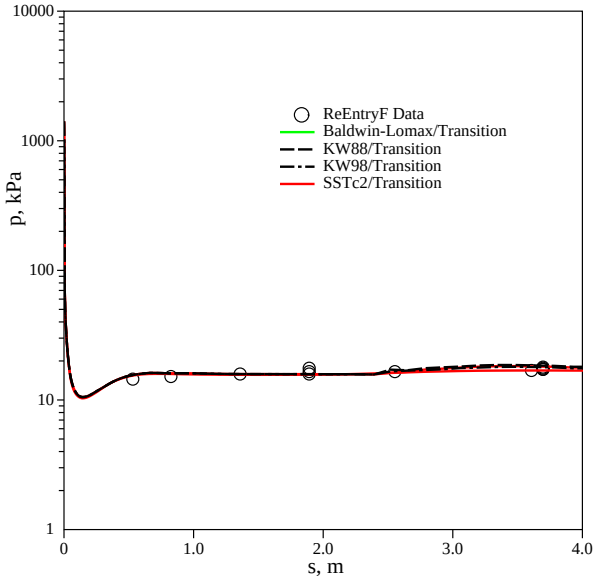

a) Wall Pressure

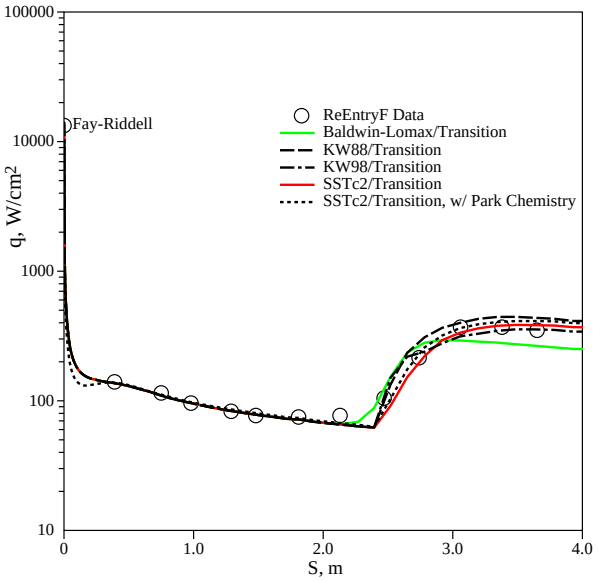

b) Heat Transfer

Fig. 19 Wall Pressure and Heat Transfer for Mach 20 ReEntry F vehicle, 24,384 m (80kft) altitude, t=456 s.

The Navier-Stokes computations for the present study are for the 24,384 m (80,000 feet) altitude ($t = 456$ s) condition. Several authors (Zoby et al.,[44] Sutton et al.,[45] and Roy and Blottner[46]) have also successfully calculated this condition using different methods, indicating a suitability of this test case for code and turbulence model validation.

For the 24,384 m (80,000 feet) altitude conditions calculated, $M_\infty = 19.97$, $T_\infty = 221.034K$, and $\rho_\infty = 0.043523$ kg/m^3, giving a unit Reynolds number of 17.9×10^6/m. The wall temperature was assumed uniform at $500K$, approximating the measurements for this altitude. Nose tip radius was given as 0.00343 m (0.1350 inches) representing a slight increase due to ablation. Transition is specified as occurring at $x = 2.80$ m. A single-block, 141×89 (streamwise $\times$ wall-normal) axisymmetric grid was used. A y^+ value of 1.0 was typical for the first grid point off the wall for those regions that are turbulent.

The Navier-Stokes solutions shown used a VL2R flux option with minmod limiter, but results with AUSM$^+$ were nearly identical. The point-Jacobi with inner relaxation time advancement option and the AF2 time advancement option also gave nearly identical results but only the calculation using the point-Jacobi option are shown.

Calculations discussed below were made using air as a perfect gas. However, as suggested by Roy and Blottner,[46] supplemental calculations, were also made with air as a dissociating real gas.

Figure 19(a) shows the wall pressure measurements which are available on the conical section only. Also shown are the wall pressure results from computations using the Baldwin-Lomax, KW88, KW98, and the SSTc2 turbulence models. The wall pressure results are virtually identical regardless of turbulence model. The computational wall pressures agree with the measurements to within 10%.

Heat transfer computations for this flight experiment obtained using the Baldwin-Lomax, KW88, KW98, and the SSTc2 turbulence models are shown in Figure 19(b) in comparison to the experimental data. The transition location is specified in these calculations so as to agree with that observed in the flight experiment. With transition location specified, the current implementation of these models in *GASP* provides agreement in heat transfer with experiment within 10%, except for the Baldwin-Lomax turbulence model. This level of agreement by these two-equation models is quite acceptable for the design of thermal protection systems provided transition can be predicted or otherwise specified. Particularly note that without the present ability to specify transition, a fully turbulent solution will significantly overpredict the total heat load on the forebody portion of the vehicle.

Possibly related to the high Mach number and low T_w/T_0 associated with this flight experiment, the Baldwin-Lomax model gives a low prediction for heat transfer level on the cone by about 30%.

Computations are also shown in Fig. 19(b) that were accomplished with the SSTc2 turbulence model using the Park[47] air chemistry model. The Park model includes 5 species (N_2, O_2, NO, N and O) with 17 reactions. With this particular real-gas chemistry model, dissociation of air will occur in the stagnation nose region, but without ionization. These computations show that along the cone, the chemistry does not particularly affect the heat transfer, $\sim 5\%$ increase on the cone. At the nose stagnation point, the inclusion of the chemistry model for air does slightly reduce the heat transfer as expected. Although there is not a strong interaction of the chemistry and turbulence for this flow, these computations do show that the SST model as implemented continues to provide accurate heat transfer results in the presence of a real-gas chemistry model.

The computed stagnation point heat transfer at the spherical nose (14.2 KW/cm^2) is the same for all of the perfect gas computations, being laminar at the nose, and agrees within 7% of the Fay-Riddell value (13.3 KW/cm^2) for the assumption of air as a perfect gas at the 24,384 m (80,000 foot) altitude condition.

Concluding Remarks

Several versions of the $k-\omega$ eddy viscosity turbulence models, including the SST and 1998 Wilcox models, along with compressibility corrections and a means to specify transition, have been incorporated into the Ames version of the real-gas Navier-Stokes *GASP* code and subjected to a validation process. The primary emphasis in this turbulence model validation process has been to evaluate the ability of the different versions of these turbulence models to predict wall heat transfer levels as required to specify thermal protection systems for planetary atmospheric entry vehicles.

The flows considered were cold-wall with Mach numbers ranging from a Mach 7, 3D experiment to an axisymmetric Mach 20 flight experiment. Complexity of experimental flows considered ranged from simple flat plates to an axisymmetric compression corner and then to a fully 3D lifting body. Real-gas effects considered included SSTc2 turbulent computations of the Mach 20 flight experiment using an air chemistry model with dissociation. Performance of the turbulence models relative to engineering correlations for flat plates was considered, as well as computational analysis of a cold-wall Mach 11.5 Helium flat-plate experiment. A Mach 7.04 compression corner experiment provided a separated strong shock/boundary-layer interaction. An experiment with a 70° sphere-cone and aftbody similar to the Mars Pathfinder was included in the turbulence model assessment.

Transition played a significant role in several of these experiments. Specification of the experimental transition location for the present transition implementation proved straightforward and without penalty as to robustness or efficiency of the solution. Incorporation of a predictive transition method is highly recommended.

The Van Leer, Roe and AUSM$^+$ upwind flux options were available for use with the $k-\omega$ models. Both the

AUSM$^+$ and the VL2R flux options performed quite well, being nearly interchangeable, with the $k-\omega$ (including the SST variants) models. However, when the Van Leer flux option was chosen for the wall-normal direction, the $k-\omega$ models would severely underpredict heat transfer. This result is counter to laminar boundary layer results with coarse grids, where specification of the Van Leer flux in the wall-normal direction is expected to give a high heat transfer due to dissipation.

A modification of the Van Leer split flux option was implemented in *GASP* so that only the mean flow equations were solved with the Van Leer split flux, whereas the turbulence equations were solved with the upwind convective flux unsplit. This modification resolved the heat transfer underprediction difficulty, providing heat transfer predictions consistent with the VL2R and AUSM$^+$ flux options. The availability of the Van Leer flux option for hypersonic flows with embedded strong shocks can be quite desirable due to the robustness of the method. The Baldwin-Lomax model, in contrast, yielded similar heat transfer results regardless of which split flux option was used.

For both the Baldwin-Lomax and the $k-\omega$ models considered, the AF2 and point-Jacobi (inner iteration) time advancement algorithms proved to be comparable as to robustness and convergence rate. The steady-state solutions were nearly identical for these two time-advancements algorithms.

Several versions of the $k-\omega$ models have proven robust and of reasonable efficiency relative to the compressible form of the widely-used Baldwin-Lomax turbulence model. Solution of the turbulence equations uncoupled from the mean flow equations provided a considerable speedup in cpu time required for a converged solution with no loss in robustness, convergence rate or solutions accuracy. The uncoupled solution procedure was possible even though physical coupling of the turbulent kinetic energy equation with the mean flow energy equation exists for hypersonic flows. For single-species calculations, the SST and KW98 turbulence models require, when solved with the uncoupled procedure, approximately 35% more cpu time per iteration than a Baldwin-Lomax solution, but without a discernible increase in the number of iterations to convergence.

The uncoupled solution procedure may be further exploited by solving the turbulence solution only every several mean flow equation iterations, with the eddy viscosity frozen between turbulence field solutions. Such a strategy reduces the overhead of using the $k-\omega$ turbulence models by 50% or more.

An assessment of the results, relative to "acreage" estimates of heat transfer, indicate that a ranking of the heat transfer accuracy and consistency for those turbulence models proven acceptable is possible, with the SST and SSTc2 models first, followed by the 1998 $k-\omega$ and the compressible Baldwin-Lomax models.

Both the standard SST model and the SST model with a modified Wilcox compressibility correction (SSTc2) consistently provide heat transfer level estimates within $+15\%$ to -5% of quality hypersonic experiments and engineering correlations. The standard SST model and the SSTc2 model do predict zero-pressure gradient heat transfer levels slightly high($\sim$ 5% to 10%), but prove to be either the most accurate or comparable in accuracy to the best of the other models for all flows considered including the aftbody and compression corner flows.

The standard 1998 $k-\omega$ and the compressible form of the Baldwin-Lomax model are comparable in their heat transfer prediction capability, providing $\pm 15\%$ accuracy, but are less consistent than the SST models with occasional significant overprediction and underprediction. Both the 1998 $k-\omega$ and Baldwin-Lomax models underpredict heat transfer for the hypersonic aftbody flow. Furthermore, the Baldwin-Lomax model overpredicts heat transfer for the leeward side of the Ames All-Body by $\sim 50\%$.

The standard 1988 Wilcox $k-\omega$ turbulence model provided heat transfer level estimates unacceptably high for the "acreage" hypersonic conditions considered. The Chien $k-\epsilon$ model as currently implemented in *GASP* provided heat transfer level estimates unacceptably low for these same hypersonic conditions. The complete modifications of Coakley and Huang[35] to the $k-\epsilon$ model for compressible flows were not implemented for the present study, however. Consideration of the Spalart-Allmaras turbulence model for hypersonic cold-wall cases was incomplete due to the inability of the model as implemented to reliably provide fully turbulent flow for these cases. However, these negative conclusions regarding the use of the Spalart-Allmaras model for hypersonic cold-wall flows do not include the possible benefits of the suggested compressible density corrections of Catris and Aupoix,[48] nor the transition modifications of Roy and Blottner.[46]

The Baldwin-Lomax, 1998 $k-\omega$, the SST and the SSTc2 turbulence models provide acceptable prediction of heat transfer levels for the separated compression corner case considered. The KW88 gives the best overall performance for the compression corner. However, none of the turbulence models correctly provides the details of the separation region. In particular, the spatial extent of separation is considerably underpredicted. Further, the heat transfer level for the early portion of separation bubble, under the λ shock region, is predicted by all turbulence models considered to initially decrease as the skin friction goes negative, whereas, experiments clearly indicate a significant increase in heat transfer immediately upon separation. Clearly, improvements in turbulence modeling are required to achieve better detail agreement with separated hypersonic compression corner flows.

Once the flow undergoes attachment, however, the predicted heat transfer levels for the compression corner are more in agreement with experiment. Peak heating levels at reattachment tended to be overpredicted by as much as 30% by all models, including the SST models. This difficulty appears related to the inability of the models to predict extent of the separation region. Heating levels past reattachment are predicted reasonably well, with the SSTc2, KW98, KW88 and Baldwin-Lomax models providing heat transfer estimates to within $\pm 15\%$ level of accuracy.

The SSTc2 turbulence model, with specified transition, provided superior performance in the calculation of heat transfer for the aftbody region of a 70° sphere-cone. Details such as heat transfer peaks associated with vortex formation in the aftbody region are accurately simulated with the SSTc2 turbulence model. No other turbulence model performed as well, with only the 1988 $k-\omega$ model, of the other models considered, able to provide heat transfer predictions within 20% of the experimental heat transfer levels.

Calculations of the Mach 20 flight experiment with air modeled either as a perfect gas or with a real-gas reacting chemistry model were accomplished. For the perfect gas computations, the SST, KW98 and KW88 turbulence models provided heat transfer predictions past transition that agreed within 10% of experiment. Turbulent computations with air modeled with a real-gas reacting chemistry model were also accomplished for this flow. Dissociation provided by the real-gas chemistry model occurs predominately in the nose region which was laminar for this flight experiment case. However, accurate turbulent heat transfer predictions (within $\sim 5\%$) along the cone surface were demonstrated in the presence of a weakly reacting flow with *GASP* using the SST turbulence model and the real-gas reacting chemistry model of Park.[47]

Summary

Strategies for establishing thermal protection system design margins favor a turbulence model that will not underpredict and only slightly overpredicts heat transfer for flows of interest. As such, the consistent accuracy in the prediction of heat transfer levels for the variety of hypersonic flows considered herein recommends consideration of the SST and the SSTc2 turbulence models for use in the computational methods employed to define aerothermal environments around proposed hypersonic atmospheric entry vehicles.

Acknowledgements

The author would like to thank William Lockman (retired NASA ARC) for providing the data in electronic form for the Ames All-Body experiment. The grids for the Ames All-Body experiment were provided by Dinesh Prabhu (Eloret). The author appreciates the positive criticism of the present work provided by Michael Wright (Eloret), Dinesh Prabhu (Eloret), Dean Kontinos (NASA ARC) and Dan Reda (NASA ARC). The author is also grateful for the opportunity to converse and absorb information pertaining to turbulence modeling from numerous co-workers, including Tom Coakley (NASA ARC), Mike Horstman (retired NASA ARC) and Joe Marvin (Eloret, retired NASA ARC). This paper was typeset using the LaTeXmacros developed by William Kleb at NASA Langley Research Center.

References

[1]Baldwin, B. and Lomax, H., "Thin Layer Approximation and Algebraic Model for Separated Turbulent Flows," AIAA Paper 78–257, Jan. 1978.

[2]Wilcox, D. C., "Reassessment of the Scale-Determining Equation for Advanced Turbulence Models," *AIAA Journal*, Vol. 26, No. 11, Nov. 1988, pp. 1299–1310.

[3]Wilcox, D. C., *Turbulence Modeling for CFD*, DCW Industries, Inc, 5354 Palm Drive, La Cañada, CA, 2nd ed., 1998.

[4]Menter, F. R., "Zonal Two Equation $k-\omega$ Turbulence Models for Aerodynamic Flows," AIAA Paper 93–2906, July 1993.

[5]Menter, F. R., "Two-Equation Eddy-Viscosity Turbulence Models for Engineering Applications," *AIAA Journal*, Vol. 32, No. 8, Aug. 1994, pp. 1598–1605.

[6]Spalart, P. and Allmaras, S., "A One-Equation Turbulence Model for Aerodynamic Flows," AIAA Paper 92–0439, Jan. 1992.

[7]Spalart, P. and Allmaras, S., "A One-Equation Turbulence Model for Aerodynamic Flows," *La Recherche Aerospatiale*, n° 1, 1994, pp. 5–21.

[8]Chien, J., "Predictions of Channel and Boundary-Layer Flows with a Low-Reynolds-Number Turbulence Model," *AIAA Journal*, Vol. 20, No. 1, Jan. 1982, pp. 33–38.

[9]AeroSoft, Inc., 1872 Pratt Drive, Blacksburg, VA 24060-6363. "GASP Version 3 Users Manual," 1996.

[10]Van Leer, B., "Towards the Ultimate Conservative Difference Scheme V. A Second-Order Sequel to Godunov's Method," *Journal of Computational Physics*, Vol. 32, No. 1, July 1979, pp. 101–136.

[11]Roe, P., "Approximate Riemann Solvers, Parameter Vectors and Difference Schemes," *Journal of Computational Physics*, Vol. 43, No. 2, Oct. 1981, pp. 357–372.

[12]Liou, M.-S., "A Continuing Search for a Near-Perfect Numerical Flux Scheme," NASA TM 106524, March 1994.

[13]Krist, S. L., Biedron, R. T., and Rumsey, C. L., "Cfl3d Users Manual (Version 5)," NASA TM 1998-208444, June 1998.

[14]Sinha, K. and Candler, G. V., "Convergence Improvement of Two-Equation Turbulence Model Calculations," AIAA Paper 98–2649, June 1998, 29th AIAA Fluid Dynamics Conference, Albuquerque, NM.

[15]Bardina, J., Huang, P., and Coakley, T., "Turbulence Modeling Validation, Testing, and Development," NASA TM 110446, April 1997.

[16]Karamcheti, K., *Principles of Ideal-Fluid Aerodynamics*, Krieger Publishing, Malabar, Florida, 2nd ed., 1980.

[17]Birch, S. and Eggers, J., "Free Turbulent Shear Flows," NASA SP 321, 1972.

[18]Sarkar, S., Erlebacher, G., Hussaini, M. Y., and Kreiss, H. O., "The analysis and modeling of dilatational terms in compressible turbulence," *Journal of Fluid Mechanics*, Vol. 227, June 1991, pp. 473–936.

[19]Zeman, O., "Dilatational Dissipation: The Concept and Application in Modeling Compressible Mixing Layers," *Physics of Fluids A*, Vol. 2, No. 2, Feb. 1990, pp. 178–188.

[20]Vuong, S. and Coakley, T., "Modeling of Turbulence for Hypersonic Flows with and without Separation," AIAA Paper 87–0286, Jan. 1987.

[21]Dhawan, S. and Narasimha, R., "Some properties of boundary layer flow during the transition from laminar to turbulent motion," *Journal of Fluid Mechanics*, Vol. 3, Jan. 1957, pp. 418–436.

[22]Van Driest, E., "Turbulent Boundary Layer in Compressible Fluids," *Journal of the Aeronautical Sciences*, Vol. 18, No. 3, March 1951, pp. 145–160,216.

[23]Van Driest, E., "On Turbulent Flow Near a Wall," *Journal of the Aeronautical Sciences*, Vol. 23, No. 11, 1956, pp. 1007–1011,1036.

[24]Van Driest, E., "The Problem of Aerodynamic Heating," *Aeronautical Engineering Review*, Vol. 15, No. 10, Oct. 1956, pp. 26–41.

[25]Rubesin, M. W. and Inouye, M., "Forced Convection, External Flows," *Handbook of Heat Transfer*, edited by W. M. Rohsenow and J. P. Hartnett, McGraw-Hill, New York, 1st ed., 1973, pp. 8–148.

[26]White, F. M., *Viscous Fluid Flow*, McGraw-Hill, New York, 1st ed., 1974.

[27]Hopkins, E. J. and Inouye, M., "An Evaluation of Theories for Predicting Turbulent Skin Friction and Heat Transfer on Flat Plates at Supersonic and Hypersonic Mach Numbers," *AIAA Journal*, Vol. 9, No. 6, June 1971, pp. 993–1003.

[28]Watson, R., "Characteristics of Mach 10 Transitional and Turbulent Boundary Layers," NASA TP 1243, Nov. 1978.

[29]Watson, R., "Wall Cooling Effects on Hypersonic Transitional/Turbulent Boundary Layers at High Reynolds Numbers," *AIAA Journal*, Vol. 15, No. 10, Oct. 1977, pp. 1455–1461.

[30]Beckwith, I. and Cohen, N., "Application of Similar Solutions to Calculation of Laminar Heat Transfer on Bodies with Yaw and Large Pressure Gradients in High Speed Flow," NASA TN D-625, 1961.

[31]Coles, D., "The Turbulent Boundary Layer in a Compressible Fluid," Rand Corp. Report R-403-PR, Sept. 1962.

[32]Kussoy, M. and Horstman, C., "Documentation of Two- and Three-Dimensional Hypersonic Shock Wave/Turbulent Boundary Layer Interaction Flows," NASA TM 101075, March 1989.

[33]Settles, G. and Dodson, L., "Hypersonic Shock/Boundary-Layer Interaction Database," NASA CR 177577, April 1991.

[34]Settles, G. and Dodson, L., "Hypersonic Shock/Boundary-Layer Interaction Database," AIAA Paper 91–1763, June 1991.

[35]Coakley, T. and Huang, P., "Turbulence Modeling for High Speed Flows," AIAA Paper 92–0436, Jan. 1992.

[36]Hollis, B., "Experimental and Computational Aerothermodynamics of a Mars Entry Vehicle," Ph. D. dissertation, North Carolina State University, 1996.

[37]Hollis, B. and Perkins, J., "Comparisons of Experimental and Computational Aerothermodynamics of a 70-deg Sphere-Cone," AIAA Paper 96–1867, June 1996.

[38]Lockman, W., Lawrence, S., and Cleary, J., "Flow over an All-Body Hypersonic Aircraft: Experiment and Computation," *Journal of Spacecraft and Rockets*, Vol. 29, No. 1, Jan.-Feb. 1992, pp. 7–15.

[39]Keyes, F., "A Summary of Viscosity and Heat Conduction Data for He, A, H2, O2, N2, CO, CO2, H2O and Air," *Transactions of the American Society of Mechanical Engineers*, Vol. 73, 1951, pp. 589–596.

[40]Lawrence, S., Chaussee, D., and Tannehill, J., "Application of an Upwind Algorithm to the Three-Dimensional Parabolized Navier-Stokes Equations," AIAA Paper 87–1112, June 1987.

[41]Prabhu, D., Wright, M., Marvin, J., Brown, J., and Venkatapathy, E., "X-33 Aerothermal Design Environment Predictions: Verification and Validation," AIAA Paper 2000–2686, June 2000, 34th AIAA Thermophysics Conference, Denver, CO.

[42]Carter, H. S., Raper, J. L., Hinson, W. F., and Morris, W. D., "Basic Measurements from a Turbulent-Heating Flight Experiment on a 5° Half-Angle Cone at Mach 20 (REENTRY F)," NASA TM X-2308, Sept. 1971.

[43]Wright, R. L. and Zoby, E. V., "Flight Measurements of Boundary-Layer Transition on a 5° Half-Angle Cone at a Free-Stream Mach Number of 20 (REENTRY F)," NASA TM X-2253, May 1971.

[44]Zoby, E., Moss, J., and Sutton, K., "Approximate Convective-Heating Equations for Hypersonic Flows," *Journal of Spacecraft*, Vol. 18, No. 1, Jan.-Feb. 1981, pp. 64–70.

[45]Sutton, K., Zoby, E., and Hamilton, H., "Overview of CFD Methods and Comparisons with Flight Aerothermal Data," *AGARD Conference Proceedings: Validation of Computational Fluid Dynamics, AGARD-CP-437*, Vol. 2.

[46]Roy, C. and Blottner, F., "Assessment of One- and Two-Equation Turbulence Models for Hypersonic Transitional Flows," AIAA Paper 2000–0132, Jan. 2000.

[47]Park, C., "On Convergence of Computation of Chemically Reacting Flows," AIAA Paper 85–0247, Jan. 1985, 23rd AIAA Aerospaces Sciences Conference.

[48]Catris, S. and Aupoix, B., "Density corrections for turbulence models," *Aerosp. Sci. Technol.*, Vol. 4, 2000, pp. 1–11.

Appendix

Several $k-\omega$ turbulence models are described in this section that are implemented in the Ames version of the *GASP* Navier-Stokes/Chemistry code. Application of these models are described in the main paper.

1988 $k-\omega$ Turbulence Model

The 1988 version of the Wilcox[2] $k-\omega$ turbulence model is:

$$\frac{D}{Dt}(\rho k) = P_k - \beta_k \rho k\omega + \frac{\partial}{\partial x_i}((\mu + \sigma_k \mu_t)\frac{\partial k}{\partial x_i}) \quad (17)$$

$$\frac{D}{Dt}(\rho \omega) = \gamma(\frac{\omega}{k})P_k - \beta_\omega \rho \omega^2 + \frac{\partial}{\partial x_i}((\mu + \sigma_\omega \mu_t)\frac{\partial \omega}{\partial x_i}) \quad (18)$$

The turbulent kinetic energy production term is:

$$P_k = \tau_{t,ij}\frac{\partial u_i}{\partial x_j} \quad (19)$$

The constitutive relation is given by:

$$\tau_{t,ij} = \mu_t((\frac{\partial u_i}{\partial x_j} + \frac{\partial u_j}{\partial x_i}) - \frac{2}{3}\delta_{ij}(\frac{\partial u_k}{\partial x_k})) - \frac{2}{3}\delta_{ij}\rho k \quad (20)$$

The turbulent dynamic viscosity is:

$$\mu_t = \rho k/\omega \quad (21)$$

The constants used for the 1988 Wilcox $k-\omega$ model are:

$$\beta_k = 0.09 \quad ; \quad \beta_\omega = 0.075; \quad (22)$$
$$\sigma_k = \sigma_\omega = 0.5 \quad ; \quad \kappa = 0.41; \text{ and,}$$

$$\gamma = \frac{\beta_\omega}{\beta_k} - \frac{\sigma_\omega \kappa^2}{\sqrt{\beta_k}} = 0.5532$$

The wall boundary conditions used, for an assumed $y^+ = 5$, are:

$$\begin{aligned} k(y=0) &= 0; \text{ and} \\ \omega(y=0) &= 100\rho u_\tau^2/\mu_w \end{aligned} \tag{23}$$

The freestream boundary conditions used are:

$$\begin{aligned} k_\infty &= 0.001U_\infty^2; \text{ and} \\ \omega_\infty &= (\sqrt{k}/L_t)_\infty \end{aligned} \tag{24}$$

Additional relations are: $\epsilon = \beta_k k\omega$; $L = \sqrt{k}/\omega$

1998 $k-\omega$ Turbulence Model

The 1998 version of the Wilcox[3] $k-\omega$ turbulence model is a modification of the earlier 1988 version. The coefficient, β_k, which determines the level of production of turbulent kinetic energy becomes dependent on the cross-diffusion derivative term, $(\partial k/\partial x_i)(\partial\omega/\partial x_i)$, so as to increase towards the outer boundary layer and for free shear layers. Additionally, the coefficient, β_ω, which determines the level of production of specific dissipation, ω, becomes dependent on the level of three-dimensionality of the flow so as to better predict axisymmetric free shear layers vs planar free shear layers.

The 1998 $k-\omega$ turbulence model makes use of the same field equations for k and ω as are used by the 1988 version. However, the constants become:

$$\sigma_k = \sigma_\omega = 0.5;\ \gamma = 0.52; \tag{25}$$

$$\beta_{k,0} = 0.09;\ \beta_{\omega,0} = 0.075;$$

$$\beta_k = \beta_{k,0} f_k;\ \beta_\omega = \beta_{\omega,0} f_\omega;$$

$$\begin{aligned} f_k &= \begin{cases} (1+680\chi_k^2)/(1+400\chi_k^2), & \text{if } \chi_k > 0, \\ 1, & \text{otherwise;} \end{cases} \\ f_\omega &= (1+70\chi_\omega^2)/(1+80\chi_\omega^2); \\ \chi_k &= ((\frac{\partial k}{\partial x_j})(\frac{\partial \omega}{\partial x_j}))/\omega^3; \\ \chi_\omega &= |\Omega_{ij}\Omega_{jk}S_{ki}|/(\omega\beta_{k,0})^3 \end{aligned}$$

The wall boundary conditions used are:

$$\begin{aligned} k(y=0) &= 0; \text{ and} \\ \omega(y=0) &= 2500\mu_w/\rho(\Delta y_1)^2 \end{aligned} \tag{26}$$

The freestream boundary conditions used are:

$$\begin{aligned} k_\infty &= 0.001U_\infty^2; \text{ and} \\ \omega_\infty &= (\sqrt{k}/L_t)_\infty \end{aligned} \tag{27}$$

The eddy viscosity is given by $\mu_t = \rho k/\omega$.

SST Turbulence Model

The SST turbulence model of Menter[4,5] is a $k-\omega$ turbulence model variation derived by merging the 1988 Wilcox[2] $k-\omega$ model applied to the inner portion of the turbulent boundary layer with a high Reynolds number form of the $k-\epsilon$ turbulence model transformed into the k and ω variables being applied to the outer portion of the turbulent boundary layer. The parameter, F_1, is defined so as to equal one for the near wall region (and through the log layer) and to vary smoothly to zero as the outer or "wake" region of the turbulent boundary layer is reached. By assigning a weight of F_1 to the inner $k-\omega$ model and a weight of $(1-F_1)$ to the outer transformed $k-\epsilon$ model, advantages of both models are incorporated into the new SST model. Additionally, the eddy viscosity relation is modified to provide a lag in development of the eddy viscosity for strong interaction flows.

The SST model is described here as:

$$\begin{aligned} \frac{D}{Dt}(\rho k) &= P_k - \beta_k\rho k\omega + \\ &\quad \frac{\partial}{\partial x_i}((\mu+\sigma_k\mu_t)\frac{\partial k}{\partial x_i}) \end{aligned} \tag{28}$$

$$\begin{aligned} \frac{D}{Dt}(\rho\omega) &= \gamma P_\omega - \beta_\omega\rho\omega^2 + \\ &\quad \frac{\partial}{\partial x_i}((\mu+\sigma_\omega\mu_t)\frac{\partial \omega}{\partial x_i}) + \\ &\quad (1-F_1)(\frac{2\rho\sigma_{\omega,2}}{\omega})(\frac{\partial k}{\partial x_i})(\frac{\partial \omega}{\partial x_i}) \end{aligned} \tag{29}$$

Where, the production terms are:

$$\begin{aligned} P_k &= \mu_t(\frac{\partial u_i}{\partial x_j})(\frac{\partial u_i}{\partial x_j}+\frac{\partial u_j}{\partial x_i}) - \frac{2}{3}\mu_t(\frac{\partial u_k}{\partial x_k})^2 \\ &\quad -\frac{2}{3}\rho k(\frac{\partial u_k}{\partial x_k}) \end{aligned} \tag{30}$$

$$\begin{aligned} P_\omega &= \rho(\frac{\partial u_i}{\partial x_j})(\frac{\partial u_i}{\partial x_j}+\frac{\partial u_j}{\partial x_i}) - \frac{2}{3}\rho(\frac{\partial u_k}{\partial x_k})^2 \\ &\quad -\frac{2}{3}\rho\omega(\frac{\partial u_k}{\partial x_k}) \end{aligned} \tag{31}$$

P_k is numerically limited to no more than 10 times the dissipation term appearing in the k equation.

The model constants are:

$$\beta_k = 0.09;\ \kappa = 0.41;\ a_1 = 0.31 \tag{32}$$

The model coefficients, $\Phi = \{\sigma_k, \sigma_\omega, \gamma, \beta_\omega\}$, are obtained by means of the blending function:

$$\Phi = F_1\Phi_1 + (1-F_1)\Phi_2 \tag{33}$$

Where, the Wilcox "inner" constants (Φ_1) are:

$$\begin{aligned} \sigma_{k,1} = 0.85;\ \sigma_{\omega,1} = 0.5; \\ \gamma_1 = 0.5532;\ \beta_{\omega,1} = 0.075, \end{aligned} \tag{34}$$

and, the "outer" constants (Φ_2) are:

$$\begin{aligned} \sigma_{k,2} = 1.00;\ \sigma_{\omega,2} = 0.856; \\ \gamma_2 = 0.4404;\ \beta_{\omega,2} = 0.0828, \end{aligned} \tag{35}$$

Two functions are needed:

$$F_1 = \tanh(\arg_1^4);\ \text{and}\ F_2 = \tanh(\arg_2^2), \tag{36}$$

Where:

$$\begin{aligned} \arg_1 &= \min(\max(\arg_{1a}, \arg_{1b}), \arg_{1c}); \\ \arg_{1a} &= \sqrt{k}/0.09\omega y; \\ \arg_{1b} &= 500\nu/\omega y^2; \\ \arg_{1c} &= 4\rho k \sigma_{\omega,2}/\mathrm{CD}_{k\omega} y^2; \\ \mathrm{CD}_{k\omega} &= \max((\frac{2\rho\sigma_{\omega,2}}{\omega}\frac{\partial k}{\partial x_i}\frac{\partial \omega}{\partial x_i}), 10^{-20}); \\ \arg_2 &= \max(2\arg_{1a}, \arg_{1b}) \end{aligned} \tag{37}$$

The eddy viscosity relation for the SST model is given by:

$$\mu_t = \rho k / \max(\omega, \Omega F_2/a_1) \tag{38}$$

Ω is the magnitude of the mean flow vorticity vector. The wall boundary conditions used are:

$$\begin{aligned} k(y=0) &= 0;\ \text{and} \\ \omega(y=0) &= 2500\mu_w/\rho(\Delta y_1)^2 \end{aligned} \tag{39}$$

The freestream boundary conditions used are:

$$\begin{aligned} k_\infty &= 0.001 U_\infty^2;\ \text{and} \\ \omega_\infty &= (\sqrt{k}/L_t)_\infty \end{aligned} \tag{40}$$